Electronic Structures of an [Fe(NNR$_2$)]$^{+/0/-}$ Redox Series: Ligand Noninnocence and Implications for Catalytic Nitrogen Fixation

Niklas B. Thompson[†], **Paul H. Oyala**[†], **Hai T. Dong**[‡], **Matthew J. Chalkley**[†], **Jiyong Zhao**[§], **E. Ercan Alp**[§], **Michael Hu**[§], **Nicolai Lehnert**[*,‡], and **Jonas C. Peters**[*,†]

[†]Division of Chemistry and Chemical Engineering, California Institute of Technology, Pasadena, California 91125, United States

[‡]Department of Chemistry and Department of Biophysics, University of Michigan, Ann Arbor, Michigan 48109-1055, United States

[§]Advanced Photon Source (APS), Argonne National Laboratory (ANL), Argonne, Illinois 60439, United States

Abstract

The intermediacy of metal-NNH$_2$ complexes has been implicated in the catalytic cycles of several examples of transition-metal-mediated nitrogen (N$_2$) fixation. In this context, we have shown that triphosphine-supported Fe(N$_2$) complexes can be reduced and protonated at the distal N atom to yield Fe(NNH$_2$) complexes over an array of charge and oxidation states. Upon exposure to further H$^+$/e$^-$ equivalents, these species either continue down a distal-type Chatt pathway to yield a terminal iron(IV) nitride or instead follow a distal-to-alternating pathway resulting in N–H bond formation at the proximal N atom. To understand the origin of this divergent selectivity, herein we synthesize and elucidate the electronic structures of a redox series of Fe(NNMe$_2$) complexes, which serve as spectroscopic models for their reactive protonated congeners. Using a combination of spectroscopies, in concert with density functional theory and correlated ab initio calculations, we evidence one-electron redox noninnocence of the "NNMe$_2$" moiety. Specifically, although two closed-shell configurations of the "NNR$_2$" ligand have been commonly considered in the literature isodiazene and hydrazido(2−) we provide evidence suggesting that, in their reduced forms, the present iron complexes are best viewed in terms of an open-shell [NNR$_2$]$^{•-}$ ligand coupled antiferromagnetically to the Fe center. This one-electron redox noninnocence resembles that of the classically noninnocent ligand NO and may have mechanistic implications for selectivity in N$_2$ fixation activity.

[*]Corresponding Authors: lehnertn@umich.edu, jpeters@caltech.edu.

Graphical Abstract

1. INTRODUCTION

Since the pioneering studies of Chatt, Hidai, and co-workers,[1] the synthesis and reaction chemistry of transition-metal complexes featuring terminal, doubly N,N-functionalized dinitrogen (N_2) ligands ("NNR_2") have been pursued because of the proposed intermediacy of $M(NNH_2)$ species in the fixation of N_2 to ammonia (NH_3).[2] In this context, the closed-shell hydrazido(2−) configuration of the "NNR_2" fragment is typically invoked to explain the susceptibility of the distal N atom (N_β) toward attack by electrophiles to produce metal hydrazidium complexes, $M(NNR_3)$, en route to N−N bond cleavage.[3] At the same time, many $M(NNR_2)$ complexes, especially those of the late transition metals, have been characterized as adducts of the charge-neutral isodiazene (NNR) oxidation state.[2b] Valence isomerization between these two closed-shell configurations−hydrazido(2−) and isodiazene −has also been proposed.[4]

Despite the prominence of Fe in the catalytic fixation of N_2,[5] the corresponding chemistry of $Fe(NNR_2)$ complexes is comparatively underdeveloped.[2b,6] Recently, we have characterized $[(P_3{}^B)Fe(NNH_2)]^+$ [$P_3{}^B$ = tris(o-diisopropylphosphinophenyl)borane] as a plausible intermediate in catalytic N_2-to-NH_3 conversion by $[(P_3{}^B{}-33)Fe(N_2)]^-$ (Figure 1).[7] Upon one-electron reduction to form the charge-neutral congener $(P_3{}^B)Fe(NNH_2)$, this species can be further protonated at N_β to yield NH_3 and a terminal iron(IV) nitride, $[(P_3{}^B)Fe{\equiv}N]^+$,[8] consistent with hydrazido(2−)-like reactivity. In comparison, the isoelectronic and isostructural complex $[(P_3{}^{Si})Fe(NNH_2)]^+$ [$P^{Si}{}_3$ = tris(o-diisopropylphosphinophenyl)silylide] appears to be stable toward protonation at low temperature.[9] Instead, this species can be further reduced to the formally 19e^- complex $(P_3{}^{Si})Fe(NNH_2)$, which disproportionates to produce complex mixtures that, most notably, include the hydrazine adduct $[(P_3{}^{Si})Fe(N_2H_4)]$. When $[(P_3{}^{Si})Fe(NNH_2)]^+$ is formed in situ and subsequently treated with substoichiometric $CoCp^*{}_2$ (Cp^* = pentamethylcyclopentadienide), high yields of both $[(P_3{}^{Si})$-$Fe(N_2H_4)]^+$ and $(P_3{}^{Si})Fe(N_2)$ are produced (Figure 1), representing, on balance, the exchange of two H atom equivalents between the $[(P_3{}^{Si})Fe(NNH_2)]^{+/0}$ redox pair to effect functionalization of the proximal N atom (N_α).[9]

Preliminary electron paramagnetic resonance (EPR) data of $(P_3^{Si})Fe(NNH_2)$ and its alkylated analogue $(P_3^{Si})Fe(NNMe_2)$ reveal significant spin density on at least a single N atom (presumably N_a), which may serve a functional role in promoting proton-coupled electron transfer (PCET) chemistry at this center.[10] Although $[(P_3^{Si})Fe(N)]^- 2$ is a comparatively inefficient catalyst for N_2 fixation,[11] we have recently proposed that similar PCET processes may play a role in increasing the efficiency of N_2 fixation by $[(P_3^B)Fe(N_2)]^-$ when using metallocene-based reductants.[12] Given this behavior, we were curious whether the electronic structures of $[(P_3^E)Fe(NNR_2)]^n$ complexes might feature a significant weight of the intermediate, open-shell hydrazyl radical anion configuration ($[NNR_2]^{•-}$) of this redox-active ligand. Although this redox state has not, to our knowledge, been explored experimentally,[13] such a proposal is reasonable given the low-energy π^* orbital of both parent and N,N-dialkylisodiazenes,[14] which thus bear a resemblance to the classically redox-noninnocent nitrosyl ligand (NO).[15] Indeed, both neutral and cationic hydrazyl radicals ($[HNNR_2]^•$ / $[H_2NNR_2]^{•+}$; R = H, alkyl) have been characterized in their free forms.[16] Such an electronic structure would be conceptually similar to that proposed for metal imidyl ($[NR]^{•-}$) and aminyl ($[NR_2]^•$) complexes that promote PCET reactivity.[10]

A detailed characterization of the electronic structures of $[(P_3^E)Fe(NNH_2)]^n$ is hampered by their high reactivity.[7–9] However, previous work has shown that the N,N-dimethylated complexes $[(P_3^E)Fe(NNMe_2)]^n$ are excellent spectroscopic models for their protonated congeners, while exhibiting greater stability.[8,9] Herein, we exploit this stability to characterize the nature of the Fe–NNMe$_2$ interaction across the $[(P_3^B)Fe-(NNMe_2)]^{+/0/-}$ redox series. This rich redox chemistry allows us to study representative complexes that are isoelectronic to each $[(P_3^B)Fe(NNH_2)]^n$ and $[(P_3^{Si})Fe(NNH_2)]^n$ species implicated thus far in N_2 fixation chemistry mediated by the $(P_3^E)Fe$ platform. Through a combination of spectroscopic and computational techniques, we demonstrate that these "hydra-zido" complexes possess ground and low-lying excited states that result from antiferromagnetic exchange coupling between the Fe and an open-shell $[NNR_2]^{•-}$ ligand. A discussion of the relevance of these electronic structures to the N_2 fixation activity of this class of complexes is presented.

2. RESULTS

2.1. Synthesis and Structural Analysis of $[(P_3^B)Fe-(NNMe_2)]^{+/0/-}$.

Like its protonated analogue, $(P^B_3)Fe(NNMe_2)$ has a diamagnetic ground state; the cyclic voltammogram (CV) of $(P_3^B)Fe(NNMe_2)$ shows a reversible oxidation centered at −1.16 V versus $Fc^{+/0}$ in tetrahydrofuran (THF).[8] Accordingly, its one-electron oxidation by $[FeCp*_2][BAr^F_4]$ ($[BAr^F_4]^-$ = tetrakis[3,5-bis(trifluoromethyl)phenyl]borate) yields $[(P_3^B)-Fe(NNMe_2)][BAr^F_4]$, which populates an S = ½ ground state (Figure 2A). $[(P_3^B)Fe(NNMe_2)]^+$ is moderately stable in the solid state and in solution but decomposes to an intractable mixture upon prolonged heating at 70 °C.

The CV of $(P_3^B)Fe(NNMe_2)$ also shows a quasi-reversible reduction centered around −2.65 V versus $Fc^{+/0}$ in THF. This couple becomes increasingly reversible at higher scan rates (Figure S34), prompting us to explore whether the reduction product could be characterized in situ at low temperature. Indeed, the reduction of $(P_3^B)Fe(NNMe_2)$ in 2-

methyltetrahydrofuran (2-MeTHF) with stoichiometric KC_8 at $-78\ °C$ produces an $S = \frac{1}{2}$ species that, on the basis of its distinctive Mössbauer and EPR properties (vide infra), can be assigned as $[(P_3{}^B)Fe(NNMe_2)]^-$ (Figure 2A). $[(P_3{}^B)Fe(NNMe_2)]^-$ is unstable, decomposing within minutes upon warming to ambient temperatures. Nevertheless, we were able to obtain a single crystal of the $[K(benzo\text{-}15\text{-}crown\text{-}5)_2]^+$ salt of $[(P_3{}^B)Fe\text{-}(NNMe_2)]^-$ suitable for X-ray diffraction [see the Supporting Information (SI) for details], confirming the structural assignment made on the basis of spectroscopy.

The solid-state structures of $[(P_3{}^B)Fe(NNMe_2)]^{+/0/-}$ determined by X-ray diffraction are shown in Figure 2B. For each complex, the "NNMe$_2$" ligand is planar $[\sum\angle(N_\beta) = 360°]$, and an approximate mirror plane is formed by P1, Fe, and N_α. The equatorial phosphine substituents of $[(P_3{}^B)Fe(NNMe_2)]^{0/-}$ adopt a slightly distorted trigonal arrangement about the Fe center with geometries intermediate between trigonal-bipyramidal and tetrahedral ($\tau = 0.34$ and 0.53, respectively).[17] Upon oxidation to $[(P_3{}^B)Fe(NNMe_2)]^+$, the P2–Fe–P3 angle widens as an η^3-B,C,C interaction forms between the Fe center and the phenylene linker of one of the phosphine substituents [$d(Fe–C1) = 2.727(3)$ Å; $d(Fe–C2) = 2.683(3)$ Å] (see Figure 2B). While the Fe–N–N angle is close to linear for the charge-neutral complex ($176.1°$), it becomes significantly bent in $[(P^B{}_3)Fe(NNMe_2)]^+$ ($159.6°$) and $[(P_3{}^B)Fe(NNMe_2)]^-$ ($161.7°$). Similar Fe–N–N angles were observed for $[(P_3{}^B)Fe\text{-}(NNH_2)]^+$ (~$150°$)[7] and $(P^{Si}{}_3)Fe(NNH_2)$ (~$151°$),[9] suggesting that these alkylated complexes are faithful structural models of their protonated analogues.

In this redox series, the Fe–N/N–N distances change in a nonlinear fashion, from $1.738(3)/1.252(4)$ Å in $[(P_3{}^B)Fe\text{-}(NNMe_2)]^+$ to $1.680(2)/1.293(3)$ Å in $(P_3{}^B)Fe(NNMe_2)$ to $1.771(7)/1.27(1)$ Å in $[(P_3{}^B)Fe(NNMe_2)]^-$. This range of N–N distances is longer than that calculated for free NNR_2 ($1.20–1.22$ Å[14c,18]) but significantly shorter than that observed for free hydrazine (1.47 Å[19]) or $M(NNR_3)$ ($1.40–1.43$ Å; R = H, alkyl[3e,20]) complexes, suggesting some degree of N–N π bonding. The Fe–N distance of $(P_3{}^B)Fe(NNMe_2)$ falls within the range observed for terminal iron imido complexes ($1.61–1.72$ Å[21]) but is longer than those observed for C_3-symmetric, terminal iron nitrides ($1.51–1.55$ Å[8,22]). The Fe–N distances of $[(P^B)Fe(NNMe_2)]^{+/-}$ are longer than those typically observed for iron imides but do fall into this range if the four-coordinate iron(III) imidyl species reported by Betley and co-workers are included (Fe–N = 1.77 Å).[10e,f]

2.2. ^{57}Fe Mössbauer Spectroscopy.

The Mössbauer spectrum of $(P_3{}^B)Fe(NNMe_2)$ has been reported in a recent communication,[8] and its parameters are collected in Table 1, along with those of related $(P_3{}^E)Fe$ complexes. While $(P_3{}^B)Fe\text{-}(NNH_2)$ has parameters very similar to those of $(P_3{}^B)Fe\text{-}(NNH_2)$ and the isostructural, silylated complex $(P_3{}^B)Fe(NN\text{-}[Si_2])$ (N$[Si_2]$ = 2,2,5,5-tetramethyl-1-aza-2,5-disilacyclopentyl), the isomer shift of the nominally isoelectronic terminal imido complex $(P_3{}^B)Fe(NAd)$ is significantly smaller than those of the $(P_3{}^B)Fe(NNR_2)$ complexes. This difference can be attributed to greater covalency in the Fe–N interaction of the imido complex,[8,11,23] which is consistent with the structural analysis given above. The Mössbauer parameters of the isoelectronic $P_3{}^{Si}$ complexes $[(P_3{}^{Si})Fe(NNR_2)]^+$ (R = H, Me) are very similar to those of their $P_3{}^B$ analogues, despite the difference in the axial ligating elements.

For the $[(P_3^B)Fe(NNMe-)]^{+/0/-}$ series, the isomer shift of the cationic complex increases by 0.14 mm s^{-1} relative to its charge-neutral congener, while that of the anionic complex increases by 0.22 mm s^{-1}, reflecting the increased Fe–N and Fe–P distances observed crystallographically. As above, the Mössbauer parameters of $[(P_3^B)Fe(NNMe_2)]^+$ are close to those reported for its protonated analogue,[7] further illustrating the utility of the alkylated complexes as spectroscopic models. Interestingly, even at temperatures as high as 80 K, $[(P_3^B)Fe(NNMe_2)]^+$ is in the limit of slow electronic relaxation, which has allowed us to estimate the ^{57}Fe hyperfine coupling (HFC) tensor from the field dependence of the spectrum (Table 1 and Figure 3A).

$[(P_3^B)Fe(NNMe_2)]^-$ also exhibits unusually slow electronic relaxation at 80 K (Figure 3B), which was observed for the isoelectronic silyl complexes $(P_3^{Si})Fe(NNR_2)$ (R = H, Me).[9] The similarity between the Mössbauer parameters of $(P_3^{Si})Fe-(NNR_2)$ (R = H, Me) and those of $[(P_3^B)Fe(NNMe_2)]^-$ (Table 1) reveals that this set of isoelectronic complexes exhibit similar electronic structures, as was observed for their one-electron-oxidized congeners above. Notably, the isotropic ^{57}Fe HFC constant (a_{iso}) of $[(P_3^B)Fe(NNMe_2)]^-$ is more than 2 times larger than that of $[(P_3^B)Fe(NNMe_2)]^+$; indeed, a similar trend in a_{iso} is observed for nearly every magnetic nucleus in the coordination sphere of Fe (vide infra). The Mössbauer parameters calculated for $[(P_3^B)Fe(NNMe_2)]^{+/-}$ via density functional theory (DFT) are in excellent agreement with the experimental ones extracted from simulation (Table 1).

2.3. Nuclear Resonance Vibrational Spectroscopy (NRVS) for the $[(P_3^B)Fe(NNMe_2)]^{+/0/-}$ Series.

To analyze in detail the changes that occur in the bonding of the Fe–NNMe$_2$ unit upon oxidation/reduction, we collected NRVS data for the full redox series, including the $[(P_3^B)^{57}Fe(^{14}N^{14}NMe_2)]^n$ and $[(P_3^B)^{57}Fe(^{15}N^{15}NMe_2)]^n$ isotopologues. This vibrational technique selectively probes motions coupled to the ^{57}Fe nucleus and, with the aid of isotopic labeling and quantum-chemistry-centered normal coordinate analysis (QCC-NCA),[24] allows us to extract force constants for the metal–ligand stretching and bending modes.

The experimental NRVS data of neutral $(P_3^B)Fe(NNMe_2)$ show two major isotope-sensitive features at 448 and 545 cm^{-1} that shift to 442 and 540 cm^{-1}, respectively, upon ^{15}N labeling. DFT calculations reproduce the NRVS data of each complex studied here particularly well and, therefore, form a reliable basis for further refinement using QCC-NCA. Figure 4A shows a comparison of the experimental and QCC-NCA spectra for $(P_3^B)Fe(NNMe_2)$. On the basis of our analysis, the band at 545 cm^{-1} corresponds to the Fe–N stretch, whereas the 448 cm^{-1} feature is the Fe–N–N out-of-plane bend. Our simulations further show that the weak features at higher energy than the Fe–N stretch, which are obscured by the background noise but clearly visible in the QCC-NCA simulation at 572 and 605 cm^{-1}, have Fe–N–N in-plane bending character. Note that, in the QCC-NCA simulations, the Fe–N–N in plane bend is distributed over multiple features in the 570–610 cm^{-1} region. Labeling of the N –CH groups with ^{13}C reveals three isotope-sensitive features in the IR spectrum of the neutral complex, at 1337, 1146, and 874 cm^{-1} (Figure S28). These same features shift upon ^{15}N labeling, demonstrating significant mode mixing between N–N and N–C vibrations, although the QCC-NCA analysis suggests that the mode at 1337 cm^{-1} is predominantly N

−N stretching, while the two lower-energy modes are dominated by the antisymmetric and symmetric N−C stretching modes, respectively. Table S24 summarizes our assignments.

In the NRVS data of $[(P_3{}^B)Fe(NNMe_2)]^-$, two isotope-sensitive bands are observed at 428 and 541 cm^{-1}, which shift to 422 and 530 cm^{-1} with ^{15}N labeling, respectively. The feature at 541 cm^{-1} belongs to a mixed Fe−N stretch and Fe−N−N in-plane bending mode, where the strong mixing between these two internal coordinates is facilitated by the now bent structure of the Fe−N−N unit. The feature at 428 cm^{-1} is assigned to the Fe−N−N out-of-plane bend based on QCC-NCA. Interestingly, the intense feature at 346 cm^{-1} in the NRVS data corresponds to a mixed N−N−C/C−N−C bend. This mode also has distinct Fe−N stretching character (19% contribution). However, in this normal mode, the two N atoms do not move, and, hence, this feature is, in fact, not ^{15}N isotope-sensitive. Figure 4B shows a comparison of the experimental and QCC NCA spectra. Owing to its thermal sensitivity, IR spectra of $[(P_3{}^B)Fe(NNMe_2)]^-$ were not collected.

In the cationic compound $[(P_3{}^B)Fe(NNMe_2)]^+$, the isotope-sensitive bands are observed at 588 and 495 cm^{-1}, which shift to 579 and 486 cm^{-1} upon ^{15}N substitution, respectively. Here, the 588 cm^{-1} feature corresponds to the in-plane bend, mixed with the Fe−N stretch. The assignment of the 495 cm^{-1} band is less clear because both the Fe−N stretching and Fe−N−N out-of-plane bending modes occur in this energy region. The QCCNCA simulations predict that 66% of the NRVS vibrational density of states (VDOS) intensity of the 495 cm^{-1} band originates from the Fe−N stretch. The feature around 348 cm^{-1} is similar in nature to that described for the anionic compound and shows distinct Fe−N stretching character. Figure 4C compares the experimental and QCC-NCA spectra, showing again excellent agreement between the simulations and experiment. IR spectra of $[(P_3{}^B)Fe(NNMe_2)]^+$ show a ^{15}N-sensitive feature at 1495 cm^{-1} and another band at 1371 cm^{-1}, the latter of which also shifts upon ^{13}C labeling of the N−CH$_3$ position (Figure S29). DFT calculations predict another feature at 1153 cm^{-1}, sensitive to both ^{15}N and ^{13}C labeling, which, however, is obscured by intense resonances from the $[BAr^F{}_4]^-$ counterion in the experimental spectra. On the basis of our analysis (Table S24), the mode at 1495 cm^{-1} corresponds mostly to N−N stretching, while the lower-energy modes are mixtures of N−N and antisymmetric N−C stretching.

Table S24 summarizes all of our assignments and compares the experimentally observed vibrational frequencies to those obtained from the QCC-NCA simulations. As is evident from the table, a very intense degree of mode mixing within the Fe−NNMe$_2$ unit is present in all three complexes, especially the cationic and anionic compounds with the bent Fe−N−N units. It is therefore not possible to draw conclusions about changes in bonding between the three complexes based solely on the vibrational energies. As discussed below in section 3.1, such conclusions rely instead on the force constants from the QCCNCA simulations, listed in Table 2 (see also Table S25).

2.4.   Low-Lying Excited States of $[(P_3{}^B)Fe(NNMe_2)]^{+/0}$.

Although $(P_3{}^B)Fe(NNMe_2)$ is a diamagnet in its ground state, preliminary variable-temperature (VT) NMR and DFT studies have evidenced the presence of a low-lying, $S = 1$ paramagnetic excited state.[8] Similar behavior was observed for the isoelectronic complex

$[(P_3^{Si})Fe(NNMe_2)]^+$ [9]. In both of these cases, fitting the VT NMR data to a simple two-state, Boltzmann-weighted magnetization function showed that these triplet states lie only 3.7 ± 0.1 and 6.7 ± 0.3 kcal mol^{-1} (1300 ± 30 and 2300 ± 100 cm^{-1}) above the diamagnetic ground states, respectively.[8,9] It is noteworthy that the entropic contributions to these energy differences appear to be small, and we have obtained a more precise estimate of the adiabatic singlet–triplet gap of $(P_3^B)Fe(NNMe_2)$ of 1266 ± 7 cm^{-1}, assuming $\Delta G \approx \Delta H$ (see the SI for details).

VT ^{15}N NMR studies of $(P_3^B)Fe(^{15}N^{15}NMe_2)$ suggest that both N_α and N_β accumulate spin density in this triplet excited state (Figure 5A). Moreover, an examination of the VT ^1H NMR data shows that the isotropic shift of the N–CH$_3$ protons is roughly an order of magnitude greater than that of any of the protons on the P_3^B ligand in the excited state (Figure 5B). For example, taking the methine protons of the isopropyl substituents on the phosphines as a reference, the influence of the Fe ion in the excited state can be quantified by a Curie factor of approximately 1×10^5 ppm K. The Curie factor of the N–CH$_3$ protons is approximately 10×10^5 ppm K, despite the fact that these protons are separated from the Fe ion by an additional bond. This striking observation suggests that significant spin density is localized on the nitrogenous ligand in the triplet excited state of $(P_3^B)Fe(NNMe_2)$.

Given the behavior of $(P_3^B)Fe(NNMe_2)$, we were curious whether $[(P_3^B)Fe(NNMe_2)]^+$ also populates an excited state of higher multiplicity at relatively low temperatures. Solution-phase VT magnetic susceptibility measurements are consistent with this hypothesis, revealing an increase of almost 1 β_e as the temperature is raised over a 140 °C range. While it is not possible to determine the excited-state multiplicity from these data alone, DFT calculations indicate that the first sextet state is significantly higher in energy than the first quartet state (see the SI). Using a two-state model similar to that above, we estimate that the quartet state lies only ~5 kcal mol^{-1} (~1700 cm^{-1}) above the doublet ground state of $[(P_3^B)Fe(NNMe_2)]^+$ from these susceptibility measurements.

2.5. EPR Studies of $[(P_3^B)Fe(NNMe_2)]^{+/-}$.

The indirect evidence for relatively large ligand-centered spin density in the triplet excited state of $(P_3^B)Fe(NNMe_2)$ motivated us to experimentally determine the spin-density distribution within the "NNMe$_2$" ligands of $[(P_3^B)Fe(NNMe_2)]^{+/-}$ using EPR-based techniques. With regard to the nature of the Fe–NNMe$_2$ interaction, these data complement the structural and vibrational data presented thus far because the complete anisotropic HFC tensor is a sensitive probe of the valence electronic structure of a particular nucleus.

The continuous-wave (CW) X-band EPR spectrum of $[(P_3^B)Fe(NNMe_2)]^+$ is shown in Figure 6, along with that of $[(P_3^B)Fe(NNH_2)]^+$, for comparison. The overall rhombicity and anisotropy of the g tensors of $[(P^B_3)Fe(NNMe_2)]^+$ closely matches that of the protonated complex $[(P^B_3)Fe(NNH_2)]^+$ (Table 3),[7] once again validating the use of the former as a spectroscopic model of the latter. This is in contrast to the g tensors of the nominally isoelectronic imido species, $[(P_3^B)Fe-(NAd)]^+$, which is significantly more anisotropic (Table 3).

The CW spectrum of $[(P_3^B)Fe(NNMe_2)]^+$ shows clear HFC to three ^{31}P nuclei at $g_1 = 2.005$. In order to measure the couplings to the rest of the magnetic nuclei in $[(P_3^B)Fe-(NNMe_2)]^+$, we turned to pulse experiments at the Q band (~34 GHz). The electron nuclear double resonance (ENDOR) spectra (Figure S12) reveal coupling to ^{11}B and three ^{31}P nuclei, as well as to two nearly equivalent ^{13}C nuclei in $[(P_3^B)Fe(NN-(^{13}CH_3)_2)]^+$. The HFCs to N_α/ N_β are quite anisotropic and were measured via hyperfine sublevel correlation (HYSCORE) spectroscopy using ^{14}N and ^{15}N isotopologues (Figures S20−S27). The complete set of ligand HFC tensors is given in Table 4. We assign the more strongly coupled N atom as N_α, and note that the $^{14}N_\alpha$ coupling at g_2 (2.089) of $A_2 = -5.7$ MHz is quite similar to that measured previously for $[(P_3^B)Fe(NNH_2)]^+$ at $g_2(2.091)$, $A_2 = -6.4$ MHz;[7] the sign of the coupling is assumed here to be negative to be consistent with the published ENDOR data for $[(P_3^B)Fe(NNH_2)]^+$. Because of the anisotropy of the hyperfine interactions, these ENDOR studies were unable to unambiguously define the complete HFC tensor for N_α of $[(P_3^B)Fe(NNH_2)]^+$, consistent with the extreme rhombicity of the analogous tensor confirmed here for $[(P_3^B)Fe(NNMe_2)]^+$ via HYSCORE spectroscopy. Similar rhombicity is also observed for the $14N_\alpha$ couplings of the anionic complex, $[(P_3^B)Fe(NNMe_2)]^-$ (Table 4).

$[(P_3^B)Fe(NNMe_2)]^-$ possesses low g anisotropy, with a **g** tensor that is quite similar to those of the isoelectronic silyl complexes, $(P_3^{Si})Fe(NNR_2)$ (R = H, Me; Table 3), reinforcing the idea that these species exhibit similar electronic structures (vide infra). Parts A and B of Figure 7 show the second-derivative CW X-band EPR spectra of $[(P_3^B)Fe(^{14}N^{14}NMe_2)]^-$ and $[(P_3^B)Fe(^{15}N^{15}NMe_2)]^-$, along with simulations. Although these simulations contain six independent HFC tensors, those of the $14/15N_\alpha$, $14/15N_\beta$, $11B$, and $31P_\gamma$ nuclei were determined independently via Q-band ENDOR and HYSCORE spectroscopy, as above (Figures S8 and S14−S19). The HFC tensors of the remaining two, more strongly coupled, ^{31}P nuclei ($^{31}P_{\alpha/\beta}$) were determined through simultaneous fitting of the X-band CW and ENDOR data (Figure S9). As can be seen from the $^{14}N-^{15}N$ difference spectrum shown in Figure 7C, the final simulation is of high quality. The complete set of ligand HFCs is given in Table 4.

Q-band ENDOR spectroscopy resolves a single ^{13}C HFC tensor for $[(P_3^B)Fe(NN(^{13}CH_3)_2)]^-$, whose isotropic component is more than twice the magnitude of the average ^{13}C coupling observed for $[(P_3^B)Fe(NN(^{13}CH_3)_2)]^+$ (Table 4). Considering that the ^{13}C nuclei are >3.8 Å from the Fe center, the magnitude of this coupling is surprisingly large, corresponding to a C 2s spin population of ~0.5%; for comparison, the most strongly coupled ^{31}P nucleus, which is bound directly to the Fe center, has a P 3s spin population of ~0.9%.[25] This observation is reminiscent of the VT ^1H NMR data presented above for $(P_3^B)Fe(NNMe_2)$. An examination of Table 4 shows that the magnitude of the isotropic ligand couplings almost uniformly increases upon two-electron reduction of $[(P_3^B)Fe(NNMe_2)]^+$ to form $[(P_3^B)Fe(NNMe_2)]^-$. The only exceptions are a single ^{31}P nucleus, which remains almost unchanged, and N_β, which has a decreased isotropic component (although the anisotropic coupling increases, vide infra). This pattern matches the observation by Mössbauer spectroscopy of nearly 2-fold-increased ^{57}Fe HFC upon reduction (vide supra).

2.6. Quantum-Chemical Calculations.

2.6.1. Preliminary Bonding Considerations.—As a free molecule, NNH_2 exhibits a planar, C_{2v} geometry.[14c] The important orbitals for interaction with a transition-metal center consist of an a_1-symmetry N_α lone pair (σ_N), a b_1-symmetry N_α lone pair (π_N), and the orthogonal b_2-symmetry π^* orbital (π^*_{NN}). The qualitative molecular orbital (MO) picture for a charge-neutral, linear $R'_3B-Fe-NNR_2$ fragment under pseudo-C_{2v} symmetry is shown in Figure 8A.

In the limit of large orbital overlap, mixing of π_N and π^*_{NN} with the $3d_{xz}$ and $3d_{yz}$ orbitals, respectively, should result in the formation of two π bonds, one "in-plane" (b_1 symmetry) and one "out-of-plane" (b_2 symmetry). This simple imide-like bonding situation could be represented by an $Fe\equiv N-NR_2$ valence bond (VB) picture;[26] however, if N_β donates its lone pair to the b_2-symmetry π bond, this will lift the degeneracy of the two orthogonal π interactions (denoted by $\Delta\varepsilon_\pi$ in Figure 8A) and produce a frontier π-orbital system isolobal to ketene,[27] i.e., an $Fe\equiv N-NR_2$ VB picture. Bending of the $Fe-N-NR_2$ angle, as observed in $[(P_3^B)Fe(NNMe_2)]^{+/-}$, is expected to result in rehybridization of the π_N lone pair, producing VB pictures corresponding to the bent imido ($Fe\equiv N-NR_2$) and isodiazene adduct ($Fe\equiv N-NR_2$) structures shown in Figure 8B.

While these VB representations apply to the case of purely covalent bond character, in the limit of small orbital overlap, the $Fe-NNR_2$ out-of-plane π bonding may be better described in terms of an exchange coupling interaction involving anti-ferromagnetic alignment of the π-symmetry electrons, that is, a formal $[NNR_2]^{\bullet-}$ configuration for the ligand. In this limit, the bonding interaction within the $Fe-NNR_2$ moiety would take on diradical character.[28]

2.6.2. DFT Calculations.—To help delineate the relative weights that the VB representations shown in Figure 8B contribute to the electronic structures of $[(P_3^B)Fe(NNMe_2)]^{+/0/-}$, we first performed a series of DFT calculations using the TPSSh functional. This approach was previously shown to be accurate in predicting Mössbauer and X-ray adsorption spectroscopy (XAS) spectra for $(P_3^B)Fe$ complexes (e.g., Table 1).[8] Starting with $[(P_3^B)Fe(NNMe_2)]^-$, the optimized Kohn–Sham wave function is significantly spin-contaminated ($\langle \hat{S}^2 \rangle = 1.02$), which is an indicator of broken-symmetry (BS) character. Indeed, an examination of the unrestricted corresponding orbitals from this calculation reveals a pair of magnetic orbitals corresponding to antiferromagnetic coupling of majority spin $3d_{yz}$ and minority spin π^*_{NN} electrons. The overlap between these two spin orbitals ($\langle \alpha|\beta \rangle = 0.89$) is in the range typically taken to correspond to metal–ligand antiferromagnetic coupling in, for example, Fe(NO) complexes,[29] thus arguing in favor of a $[NNMe_2]^{\bullet-}$ configuration for the "hydrazido" ligand. In accordance with the qualitative MO diagram of Figure 8A, the uncoupled metal-based singly occupied molecular orbital (SOMO) is of $3d_{xz}$ character (Figure 9A).

At this level of theory, only a closed-shell singlet configuration could be converged for $(P_3^B)Fe(NNMe_2)$ in its ground state. Similarly, an unrestricted calculation of $[(P_3^B)Fe(NNMe_2)]^+$ is relatively spin-uncontaminated, corresponding to a normal two-electron $3d_{yz}/\pi^*_{NN}$ interaction ($27E8\langle \alpha|\beta \rangle = 0.97$). However, given that BS DFT calculations are highly sensitive to the percentage of Hartree–Fock exchange incorporated in

the exchange-correlation functional, these results are ambiguous. For example, increasing the Hartree−Fock exchange from 10% to 25% (a value closer to that typically used in BS-DFT studies[29]) results in BS (antiferromagnetic) wave functions for both $(P_3{}^B)Fe-(NNMe_2)$ and $[(P_3{}^B)Fe(NNMe_2)]^+$ in their ground spin states ($\langle a|\beta \rangle = 0.85$ and 0.90 for the $3d_{yz}/\pi^*_{NN}$ interaction, respectively). Using 25% exact exchange in the calculation decreases the corresponding overlap integral to 0.70 for $[(P_3{}^B)Fe(NNMe_2)]^-$.$\rangle$

Repeating these calculations for the low-lying triplet and quartet excited states of $(P_3{}^B)Fe(NNMe_2)$ and $[(P_3{}^B)Fe-(NNMe_2)]^+$, respectively, produces BS solutions similar to that of $[(P_3{}^B)Fe(NNMe_2)]^-$ (Figure 9B,C). The antiferromagnetic nature of the out-of-plane Fe−NNMe_2 π bonding persists, although in the case of $[(P_3{}^B)Fe(NNMe_2)]^+$, the strength of the magnetic coupling increases, reflected by the enhanced orbital overlap ($\langle a|\beta \rangle = 0.94$).[30] In the optimized structures of these redox and spin states, the Fe−N−N angle is significantly bent (156−164°), which can be rationalized by population of the $3d_{xz}$ orbital, which would result in a strongly antibonding in-plane π interaction with the π_N electrons in a linear geometry. Once more, the strength of the magnetic coupling between the $3d_{yz}/\pi^*_{NN}$ electrons is highly sensitive to the amount of exact exchange included in the calculation. The corresponding overlapintegrals decrease to 0.74 and 0.89 for $(P_3{}^B)Fe(NNMe_2)$ ($S = 1$) and $[(P^B{}_3)Fe(NNMe)]^+$ ($S = 3/2$), respectively, upon an increase in the the percentage of Hartree−Fock from 10% to 25%.

2.6.3. Complete-Active-Space Self-Consistent-Field (CASSCF) Calculations.

—To resolve this ambiguity, we turned to wave-function-based calculations. In contrast to approximate, single-reference methods like BS DFT, multireference techniques such as the CASSCF method can properly represent open-shell singlet wave functions, as well as more general cases of metal−ligand exchange coupling.

From a ground-state-specific calculation of $(P_3{}^B)Fe-(NNMe_2)$, some multireference character is evident, with the closed-shell configuration

$$\left| \left(3d_{xy}\right)^2 \left(3d_{x^2-y^2}\right)^2 \left(3d_{xz} + \pi_N\right)^2 \left(3d_{z^2} + 2p_z\right)^2 \left(3d_{yz} + \pi^*_{NN}\right)^2 \right\rangle$$

composing 79.8% of the zeroth-order wave function. The antiferromagnetic nature of the remaining determinants is hinted at from localization of the active space orbitals, which results in strong spatial separation of the Fe $3d_{yz}$ and π^*_{NN} orbitals (Figure 10).[28c,d] A quantitative measure of the antiferromagnetic character of the $3d_{yz}/\pi^*_{NN}$ interaction can be obtained from the occupation numbers of the corresponding bonding and antibonding natural orbitals ($n_\pm$). Table 5 compiles an index of the diradical character (Y) of these interactions, with $Y = 0$ corresponding to a pure two-electron bond and $Y = 1$ corresponding to a pure diradical.[28b] In this case, the significant diradical character of $3d_{yz}/\pi^*_{NN}$ interaction (17%) is consistent with the presence of a spin-coupled $[NNMe_2]^{\bullet-}$ ligand in the singlet ground state of $(P_3{}^B)Fe(NNMe_2)$. Comparable diradical character (20−30%) is found from in the π bonding of porphyrin-supported Fe(NO) complexes.[28c]

Repeating these calculations for $[(P_3^B)Fe(NNMe)]^+$ in its ground state results in a 50% decrease in the diradical character of the $3d_{yz}/\pi^*_{NN}$ interaction (Table 5), concomitant with an increase in the single-reference character (about 85%) of the zeroth-order wave function. If we, somewhat arbitrarily, take a diradical index $Y < 10\%$ as indicative of an essentially closed-shell interaction, then the dominant VB picture for $[(P_3^B)Fe-(NNMe_2)]^+$ in its ground state would be that of either a bent imido or an isodiazene adduct, with the distinction between the two determined by the degree of covalency. A Löwdin population analysis of the in-phase (bonding) $3d_{yz} + \pi^*_{NN}$ natural orbital reveals modest π^*_{NN} character (9.7%), compared with that of singlet $(P_3^B)Fe(NNMe_2)$ (27%), for example. This electronic structure is thus perhaps most consistent with the presence of an isodiazene ligand, activated by some degree of π back-bonding.

For completeness, we have also computed the zeroth-order CASSCF wave function for $[(P_3^B)Fe(NNMe_2)]^-$ and the excited states of $[(P_3^B)Fe(NNMe_2)]^{+/0}$. Consistent with the BS DFT calculations presented above, $[(P_3^B)Fe(NNMe_2)]^-$ and the $S = 1$ state of $(P_3^B)Fe(NNMe_2)$ are characterized by a large degree of diradical character in the out-of-plane π-bonding interaction; the $S = ^3/_2$ state of $[(P_3^B)Fe(NNMe_2)]^+$ appears to represent an intermediate case, with enhanced diradical character relative to the $S = \frac{1}{2}$ ground state but less than that found in singlet $(P_3^B)Fe(NNMe_2)$ (Table 5). This result is also consistent with our BS DFT calculations, which suggest stronger antiferromagnetic coupling for this redox and spin state.

The optical spectra of $(P_3^B)Fe(NNMe_2)$, $[(P_3^{Si})Fe-(NNH_2)]^+$, and $[(P_3^{Si})Fe(NNMe_2)]^+$ all exhibit transitions in the range from 12500 to 13500 cm^{-1} and from 18000 to 19000 cm^{-1}, which we presume are due to transitions involving the common Fe–NNR$_2$ core. Therefore, to judge whether these multi reference calculations provide an accurate basis for the static correlation effects in the bonding of $(P_3^B)Fe(NNMe_2)$, we have used the state-averaged (SA-)CASSCF approach to compute low-lying singlet excited states. As shown in Figure 11, at the SA-CASSCF level, the ab initio electronic spectrum is in qualitative agreement with the experimental spectrum of $(P_3^B)Fe(NNMe_2)$, although there is a systematic error in the computed transition energies of ~3000 cm^{-1}. Accounting for dynamic correlation through a second-order N electron valence perturbation theory (NEVPT2) calculation on top of our SACASSCF reference brings the ab initio spectrum into almost quantitative agreement with experiment, especially considering that we have ignored environmental effects (e.g., solvent). This latter calculation indicates that our chosen complete active space is well-balanced. On the basis of these calculations, we can assign the optical transitions of $(P_3^B)Fe(NNMe_2)$ as being principally due to transitions from the filled $3d_{xy}$ and $3d_{x2-y2}$ orbitals into the $(3d_{xz} - \pi_N)$ and $(3d_{yz} - \pi^*_{NN})$ orbitals, as postulated (Table S15).

To evaluate the accuracy of our approach for $[(P_3^B)Fe-(NNMe_2)]^{+/-}$, at least in their ground states, we have used the **g** tensor as a measure because it is quite sensitive to the valence electronic structure. As can be seen in Table 6, the **g** tensors computed using a SA-CASSCF reference are in good agreement with experiment. We have also computed the anisotropic parts of the ^{14}N HFC tensors, collected in Table 6. For $[(P_3^B)Fe-(NNMe_2)]^-$, the computed hyperfine parameters are in excellent agreement with those determined via HYSCORE spectroscopy, in terms of both their magnitude (t) and rhombicity (δ_{HFC}; eq S11). Given that

we have neglected dynamic correlation in these calculations, our results indicate that the antiferromagnetic interaction identified above dominates the valence electronic structure of $[(P_3{}^B)Fe(NNMe_2)]^-$. For $[(P_3{}^B)Fe(NNMe_2)]^+$, the agreement is poorer, although the absolute errors remain small. This suggests that neglecting dynamic correlation leads to a worse approximation for this redox state.

3. DISCUSSION

3.1. Nature of the Fe–NNMe$_2$ Interaction as a Function of the Redox and Spin States.

We begin our discussion in terms of the ground spin states of $[(P_3{}^B)Fe(NNMe_2)]^{+/0/-}$. In the foregoing, we assume covalent Fe–B bonding, which increases the formal Fe valence by 2, although there is evidence supporting the redox activity of this interaction (vide infra). From the solid-state structures, the Fe–N bond distance follows the trend $(P_3{}^B)Fe(NNMe_2)$ < $[(P_3{}^B)Fe(NNMe_2)]^+$ < $[(P_3{}^B)Fe(NNMe_2)]^-$. This trend is mirrored in the Mössbauer isomer shifts, suggesting that the Fe–NNMe$_2$ bonding is strongest in the charge-neutral complex and weakest in the anionic complex. The Fe–N stretching force constants extracted by NRVS measurements quantify this effect (Table 2). By contrast, our vibrational analysis reveals that the N–N stretching force constant follows the trend $[(P_3{}^B)Fe(NNMe_2)]^+$ > $(P_3{}^B)Fe(NNMe_2) \approx [(P_3{}^B)Fe(NNMe_2)]^-$. Therefore, while the first reduction has a significant effect on the N–N bonding, the formal configurations of the "NNMe$_2$" moieties of the neutral and anionic complexes appear to be the same.

These two trends can be rationalized by consideration of the Fe–N–N angles in these complexes. In a linear geometry, two π-bonding interactions are possible within the Fe –NNMe$_2$ unit (vide supra). The presence of a strong in-plane π bond in $(P_3{}^B)Fe(NNMe_2)$ is demonstrated by the large in-plane Fe–N–N bending force constant of 1.98 mdyn Å for this complex. In the bent geometries of $[(P_3{}^B)Fe(NNMe_2)]^+$ and $[(P_3{}^B)Fe(NNMe_2)]^-$, this drops to 0.59 and 0.68 mdyn Å, respectively. Given that rehybridization of the in-plane N_α lone pair should have no effect on the orthogonal N–N π bonding, this effect explains why the Fe –N force constants of the neutral and anionic complexes are so different despite the fact that their N– N force constants are identical.

The N–N force constant of NNH is 11.7 mdyn Å^{-1} from ab initio calculations,[31] compared with 8.55 mdyn Å^{-1} measured for $[(P_3{}^B)Fe(NNMe_2)]^+$. This latter value is significantly higher than the N–N force constants measured either for a trans-N_2H_2 ligand bridging two Fe^{II} centers (7.73 mdyn Å^{-1}),[32] or for $[(dppe)_2(F)W(NNH_2)]^{+\cdot}$ (7.20 mdyn Å^{-1}),[33] which was described as an isodiazene adduct. *Thus, $[(P_3{}^B)Fe(NNMe_2)]^+$ is best viewed as a low-spin, iron(III) isodiazene adduct.* The rather large Fe–N force constant for this complex is then the result of both strong σ donation and π back-bonding. This formulation is consistent with our ab initio calculations, showing relatively low antiferromagnetic character and relatively low covalency in the out-of-plane π interaction.

In $(P_3{}^B)Fe(NNMe_2)$ and $[(P_3{}^B)Fe(NNMe_2)]^-$, the N–N stretching force constant is reduced to 6.8 mdyn Å^{-1}, which is intermediate between that of $[(dppe)_2(F)W(NNH_3)]^{2+}$ and that of $[(dppe)_2(F)W(NNH_3)]^{2+}$ (6.03 mdyn Å^{-1}).[34] This indicates only partial reduction of the N –N π bond, in line with our crystallographic analysis. Moreover, the significantly lower

isomer shift of $(P_3^B)Fe(NAd)$ versus $(P_3^B)Fe(NNMe_2)$ indicates that the "amino–imido" VB picture of Figure 8B has relatively low weight for the latter complex. While a purely hydrazido(2−) configuration is thus incompatible with our observations, these data alone do not shed light on the possible open-shell character of the "$NNMe_2$" ligand of these complexes.

The presence of a spin-coupled ligand radical in $[(P_3^B)Fe-(NNMe_2)]^-$ is, however, supported by EPR spectroscopy. Naturally, some spin density is expected at the "$NNMe_2$" ligand because of polarization by Fe-centered spin. To gauge the effect of spin polarization on the N-centered spin density, we can take the anisotropic HFCs measured for $[(P_3^B)Fe(NNMe_2)]^+$, $t(^{14}N_\alpha) = -2.5$ and $t(^{14}N_\beta) = -1.9$ MHz, as a reference. Upon two-electron reduction to $[(P_3^B)Fe(NNMe_2)]^-$, the magnitude of the π-centered spin density on N_α increases by more than a factor of 4 (−11.1 MHz). While the increase in t for N_β is relatively small (−2.4 MHz), the isotropic ^{13}C coupling for the N−CH_3 group increases to the range expected for a methyl group bound to a π radical (19.6 MHz). For example, $a_{iso}(^{13}C) = 38$ MHz for the sp^3 carbon nucleus of the ethyl radical.[35] While the ^{13}C HFC constants of known *N,N*-dimethylhydrazyl radicals have not been determined, we can compare this to $a_{iso}(^{13}C) = 37$ MHz calculated by DFT methods for $[NNMe_2]^{•-}$ in its equilibrium geometry and $a_{iso}(^{13}C) = -22$ MHz in a planar geometry resembling that observed crystallographically for the "$NNMe_2$" ligand of $[(P_3^B)Fe(NNMe_2)]^-$. The anisotropic $^{14}NHFC$ constants calculated in this fashion for $[NNMe_2]^{•-}[t(^{14}N_\alpha) = 32.0/33.3$ and $t(^{14}N_\beta) = 7.3/11.0$ MHz in the equilibrium/planar geometries] are also on the same order as those measured experimentally for $[(P_3^B)Fe(NNMe_2)]^-$.

It may be argued that these effects are due to changes in the symmetry of the metal-based SOMO upon reduction. That is, greater orbital overlap between the SOMO and N_α p orbitals would result in greater delocalization of the majority (α) spin onto the ligand, which should produce enhanced polarization of the local minority (β) spins. However, for this explanation to hold, one would expect the isotropic ^{57}Fe HFC to decrease upon reduction, in accordance with enhanced covalency. Instead, as shown by the magnetically perturbed Mössbauer spectra, it more than doubles. At the same time, the isotropic parts of both the ^{11}B and average ^{31}P HFCs also increase. It is challenging to reconcile all of these observations simultaneously in terms of a simple $S = ½$ metalloradical picture for both $[(P_3^B)Fe-(NNMe_2)]^+$ and $[(P_3^B)Fe(NNMe_2)]^-$.

On the other hand, these trends can be simply rationalized in terms of an exchange-coupling model of the bonding in $[(P_3^B)Fe(NNMe_2)]^-$. In this framework, the $S_{tot} = ½$ ground state of $[(P_3^B)Fe(NNMe_2)]^-$ results from antiferromagnetic coupling between an intermediate-spin, $S = 1$ Fe^{II} center and a $S = ½$ $[NNMe_2]^{•-}$ ligand. The incomplete magnetic coupling between these two centers would be expected to result in a more diffuse distribution of the spin density, as is observed. This effect is visualized in the CASSCF-calculated spin densities (Figure 12), in which the magnitudes of the α spin density on Fe (in excess of that expected on the basis of S) and the β spin density on N_α are seen to be correlated to the antiferromagnetic character of the Fe−$NNMe_2$ bonding.

Thus, in agreement with our quantum-chemical calculations, [(P₃ᴮ)Fe(NNMe₂)]⁺ is best considered as containing a spin-coupled [NNMe₂]•⁻ ligand. By inference, (P₃ᴮ)Fe(NNMe₂) is most concisely described as a low-spin Fe^{III} center ($S = {}^1/_2$) coupled antiferromagnetically to an $S = ½$ [NNMe₂]•⁻ ligand, as suggested by CASSCF and the similarly low N−N force constant of this compound. Compared to the neutral compound, one-electron reduction leads to an occupation of the in-plane, π-antibonding $3d_{xz}$ orbital in [(P₃ᴮ)Fe(NNMe₂)]⁻, which explains the dramatic drop in the Fe−N force constant in the reduced complex and the bending of the Fe−N−N unit (due to Coulomb repulsion with the N_α in-plane lone pair), while leaving the N−N bonding mostly unaffected.

While detailed vibrational and EPR-based studies of the triplet excited state of (P₃ᴮ)Fe(NNMe₂) are not possible experimentally, the indirect observation of significant ligand-centered spin density in this excited state by VT NMR is also consistent with the presence of a [NNMe₂]•⁻ ligand. From our calculations, the strength of the antiferromagnetic coupling follows the trend (P₃ᴮ)Fe(NNMe₂) ($S = 0$) > [(P₃ᴮ)Fe(NNMe₂)]⁻ ($S = ½$) > (P₃ᴮ)Fe(NNMe₂) ($S = 1$). As discussed above, the quartet excited state of [(P₃ᴮ)Fe(NNMe₂)]⁺ represents a more ambiguous case. On the basis of our calculations, this state appears to contain significant contributions from both NNMe₂ and [NNMe₂]•⁻ configurations of the ligand.

3.2.   Implications for N₂ Fixation Activity.

Combined with our previous work,[8,9] the studies presented here demonstrate that the N-alkylated complexes [(P₃ᴱ)Fe-(NNMe₂)]^n serve as faithful electronic models of their N-protonated congeners, as judged by EPR, Mössbauer, NMR, UV−vis, and XAS spectroscopies. Moreover, when making isoelectronic comparisons, the (P₃ᴮ)Fe complexes do not appear to differ meaningfully from those supported by the P₃^{Si} ligand, leading us to propose analogous electronic structures.

So, the question naturally arises, do the electronic structures of the title compounds rationalize the differential reactivity of the isoelectronic complexes (P₃ᴮ)Fe(NNH₂) and [(P₃^{Si})Fe-(NNH₂)]⁺ in the context of N₂ fixation?

Assigning an [NNH]•⁻ oxidation state to the "NNH₂" ligand of (P₃B)Fe(NNH₂) may seem at odds with its apparent susceptibility toward protonation at N_β to yield NH₃ and [(P₃ᴮ)Fe≡N]⁺,[8] although it should be noted that the dominant resonance structure of [NNH]•⁻ results in lone-pair character on N_β. Moreover, in (P₃ᴮ)Fe(NNH₂), additional reducing equivalents are harbored in the redox-active Fe−B interaction. According to CASSCF calculations, the diradical character of this interaction varies from $Y = 0.11$ in singlet (Pᴮ₃)Fe(NNMe₂) to $Y = 0.21$ in its triplet excited state. This result is surprising, given the σ symmetry of this interaction, and testifies to the electronic flexibility of the Fe−B bond. Thus, as N_β becomes protonated, N−H bond formation can be facilitated by transfer of these electrons to the "NNH₂" unit. From this perspective, the protonation reaction could be viewed as a form of intra-molecular PCET. This flow of electrons is consistent with the XAS/time-dependent DFT characterization of [(P₃ᴮ)Fe≡N]⁺,[8] which shows that the lowest unoccupied molecular orbital of the system is an a_1-symmetry orbital of dominant ($3d_z{}^2$ + B $2p_z$) character−i.e., the B atom becomes oxidized in the transformation shown in Figure 13A. Our proposal here is

consistent with previous observations made by us[8] and the conclusions reached in a recent computational study.[36] In essence, the compound is able to store additional reducing equivalents in the Fe−B bond, which can then be utilized to cleave the N−N bond and form the first equivalent of NH_3.

This behavior helps to explain why a similar N−N bond cleavage reaction is not observed for $[(P_3{}^{Si})Fe(NNH_2)]^+$. From a coarse-grained perspective, the stability of this species toward protonation can be rationalized in terms of electrostatic effects. That is, owing to its cationic nature, one would expect the N_β atom of $[(P_3{}^{Si})Fe(NNH_2)]^+$ to be less basic than that of $(P_3{}^B)Fe(NNH_2)$.[37] However, we can reformulate this statement in terms of the reducing power of the silyl ligand. That is, protonation at N_β and N−N bond cleavage would produce an iron(IV) nitrido in which the silyl ligand becomes oxidized to $[R_3Si]^+$ (Figure 13B). Because the $[R_3Si]^{\bullet/+}$ couple occurs at much higher potentials than the corresponding $[R_3B]^{\bullet-/0}$ couple, one would expect this transformation to be more challenging for the $P_3{}^{Si}$ ligand compared with the $P_3{}^B$ ligand. If the Fe−Si bonding is substantially more covalent than the Fe−B bonding, then the Fe center would have to provide the reducing equivalents necessary for N−N bond cleavage, producing a formal Fe^{VI} oxidation state, which should occur at similarly high potentials.

Although $[(P_3{}^{Si})Fe(NNH_2)]^+$ is thus stable to protonation, it can be reduced to $(P_3{}^{Si})Fe(NNH_2)$ by $CoCp^*{}_2$ (Figure 13B). As discussed in the Introduction, mixtures of $[(P_3{}^{Si})Fe-(NNH_2)]^{+/0}$ decay upon warming to produce high yields of $[(P_3{}^{Si})Fe(N_2H_4)]^+$, in which N_a, rather than N_β, has been functionalized (Figure 1).[9] On the basis of EPR studies of $[(P_3{}^B)Fe(NNMe_2)]^-$, which is isoelectronic to $(P_3{}^{Si})Fe-(NNH_2)$, in this redox state, the distribution of N-centered spins should be weighted in favor of N_a $[|t(N_a)/t(N_\beta)| \approx 5]$, which would explain preferential N_a functionalization if N−H bond formation occurs via H-atom transfer (HAT). Either $[(P_3{}^{Si})Fe(NNH_2)]^+$ or $(P_3{}^{Si})Fe(NNH_2)$ could serve as a suitable HAT donor, given the extremely weak N−H bonds of these species (bond dissociation energies estimated to be 49 and 37 kcal mol^{-1}, respectively).[12b,38] It should also be noted that the bending of the Fe−N−N angle is accompanied by greater lone-pair character at N_a (vide infra), and N−H bond formation via a proton-transfer or PCET mechanism is thus also conceivable.

Given the low potential of the $[(P_3{}^B)Fe(NNMe_2)]^{0/-}$ couple (ca. −2.7 V), we do not expect $[(P_3{}^B)Fe(NNH_2)]^-$ to be a relevant oxidation state in catalytic N_2 fixation by $[(P_3{}^B)Fe-(N_2)]^-$ using our most efficient conditions in which $CoCp^*{}_2$ is the reductant ($E^{\circ\prime}$ = −2.1 V).[12a] However, on the basis of the results above, the $[(P_3{}^B)Fe(NNH_2)]^+$ and $(P_3{}^B)Fe(NNH_2)$ redox states should possess low-lying paramagnetic excited states that are characterized by weakened antiferromagnetic metal−ligand coupling. Indeed, the similarity between these excited states and the most reduced state, at least from the perspective of the $[NNH_2]^{\bullet-}$ ligand (cf. Figure 12), suggests that population of these states under catalytic conditions could engender "$(P_3{}^{Si})$Fe-like" reactivity, that is, a preference for a distal-to-alternating mechanism producing N_2H_4,[9] rather than a purely distal mechanism producing NH_3.[8] While direct thermal population of these states seems unlikely at the low temperatures relevant to catalysis (−78 °C), it may be possible to access similar electronic structures photochemically (cf. Figure 11).

4. CONCLUSION

Herein, we have provided experimental and theoretical evidence supporting the formulation of the reduced $[(P_3^B)Fe(NNR_2)]^{0/-}$ complexes as containing a $[NNR_2]^{\bullet-}$ ligand coupled antiferromagnetically to the Fe center. This characterization completes the set of "NNR_2" redox states commonly considered in $M(NNR_2)$ complexes: isodiazene, hydrazido(2−), and, now, hydrazyl radical anion. On the other hand, the cationic complex, $[(P_3^B)Fe(NNR_2)]^+$, is best described as a "classic" isodiazene complex, similar to the Chatt-type $[("P")_4Mo(II) (NNH_2)]^{2+}$ systems.[33] In many ways, this mirrors the redox activity of the nitrosyl ligand, which can be present in $[NO]^+$, $NO^{\bullet}$, or $[NO]^-$ oxidation states.

The one-electron redox noninnocence of the "NNR_2" ligand may manifest itself in other examples of transition-metal-mediated N_2 fixation. For example, a key intermediate proposed in the catalytic cycle of Schrock's triamidoamine-supported Mo catalyst is a cationic, formally Mo^{VI}, $[Mo(NNH_2)]^+$ complex; upon reduction to a putative Mo(V) hydrazido complex, this species undergoes a complex series of disproportionation reactions, yielding mixtures of Mo(NNH), Mo≡N, and $[Mo(NH_3)]^{+/0}$.[39] This chemistry is formally similar to that which occurs upon the reduction of $[(P_3^{Si})Fe(NNH_2)]^+$[9] and may have a common physical basis. Although the molybdenum-(V) "hydrazido" complex has not been observed experimentally, DFT studies suggest that the Mo-based SOMO is the repulsive $4d_{xz}$ orbital,[40] causing a bending of the Mo−N−N angle, quite analogous to the reduction of $(P_3^B)Fe(NNMe_2)$ to $[(P_3^B)Fe(NNMe_2)]^-$ [or the reduction of $[(P_3^{Si})Fe(NNH_2)]^+$ to $(P_3^{Si})Fe(NNH_2)$]. While it has not been considered explicitly in the literature, our results suggest that an electronic structure consisting of a high-spin Mo^{IV} ion ($S = 1$) antiferromagnetically coupled to a $[NNH_2]^{\bullet-}$ ligand should be considered for this complex. More broadly, given the central role of $M(NNR_2)$ complexes in the catalytic fixation of N_2, potentially including even biological N_2 fixation,[41] the elucidation of their electronic structures remains an important goal.

5. EXPERIMENTAL SECTION

General Considerations.

Unless noted otherwise, all manipulations were carried out using standard Schlenk or glovebox techniques under a N_2 atmosphere. Solvents were deoxygenated and dried by a thorough sparging with N_2, followed by passage through an activated alumina column in a solvent purification system by SG Water, USA LLC. Deoxygenated, anhydrous 2-MeTHF was purified by stirring over sodium−potassium alloy and filtering through a short column of activated alumina prior to use. Nonhalogenated solvents were tested with sodium benzophenone ketyl in THF in order to confirm the absence of oxygen and water. Deuterated solvents were purchased from Cambridge Isotope Laboratories, Inc., degassed, and dried over activated 3 Å molecular sieves prior to use.

The compounds $(P_3^B)^{57}Fe(Cl)$[8], $(P_3^B)Fe(NNMe_2)$,[8] $(P_3^B)Fe(NN[Si])$,[6c] and $[(P_3^B)Fe(NAd)] [BAr^F_4]$[7] were prepared according to literature procedures. All other reagents were purchased from commercial vendors and used without further purification unless otherwise stated.

Spectroscopic Methods.

NMR spectra were collected on a 500 MHz instrument from Varian; chemical shifts for ^1H are reported in ppm relative to tetramethylsilane, using resonances from residual solvents as internal standards; ^{15}N resonances are reported in ppm relative to the chemical shift of $^{15}NH_3(liq)$, referenced to the signal of the deuterated solvent used to lock the instrument. IR measurements were obtained as powders or thin films formed by the evaporation of solutions using a Bruker Alpha Platinum ATR spectrometer with OPUS software. Optical spectroscopy measurements were collected with a Cary 50 UV−vis spectrophotometer using a 1 cm two-window quartz cell. VT measurements were collected with a Unisoku CoolSpek cryostat mounted within the Cary spectrophotometer.

Mössbauer spectra were recorded on a spectrometer from SEE Co. (Edina, MN) operating in the constant-acceleration mode in a transmission geometry. The sample was kept in an SVT-400 cryostat from Janis (Wilmington, MA), using liquid N_2 as a cryogen for 80 K measurements. Magnetically perturbed spectra were recorded in the presence of a 50 mT permanent magnet, aligned either parallel or perpendicular to the direction of γ-ray propagation. The quoted isomer shifts are relative to the centroid of the spectrum of a metallic foil of α-Fe at room temperature. Solution samples were transferred to a sample cup, chilled to 77 K inside of the glovebox, quickly removed from the glovebox, and immersed in liquid N_2 until mounted in the cryostat. Data analysis was performed using version 4 of the program *WMOSS* (www.wmoss.org).[42] Additional simulation details are available in the SI.

NRVS data were obtained as described previously at Beamline 3ID at the APS at ANL.[43] Samples were loaded in copper sample holders with lucite lids. During data collection, samples were maintained at cryogenic temperatures using a liquid-He-cooled cryostat. Spectra of solid samples were recorded from −50 to +120 meV in 0.25 meV steps. Multiple scans were taken, normalized to the intensity of the incident beam, and added together to achieve adequate signal-to-noise; the final spectra represent averages between 4 and 10 scans. The program *Phoenix* was used to convert the raw NRVS data to the VDOS.[44]

X-band (9.4 GHz) CW EPR spectra were acquired using a Bruker EMX spectrometer equipped with a Super High-Q (SHQE) resonator using Bruker *Win-EPR* software (version 3.0). Spectra were acquired at 77 K using a vacuum-insulated quartz liquid-N_2 immersion dewar inserted into the EPR resonator. Spectra were simulated using the *EasySpin* simulation toolbox (release 5.2.15) with *Matlab R2016b*. All pulse X-band (9.7 GHz) and Q-band (34 GHz) EPR, HYSCORE, and ENDOR spectra were acquired using a Bruker ELEXSYS E580 pulse EPR spectrometer equipped with a Bruker MD4 (X-band) or D2 (Q-band) resonator. Temperature control was achieved using an ER 4118HVCF5-L Flexline Cryogen-Free VT cryostat manufactured by ColdEdge equipped with an Oxford Instruments Mercury ITC temperature controller. Spectra were simulated using the *EasySpin* simulation toolbox (release 5.2.15) with *Matlab R2016b*. Additional data collection and simulation details are available in the SI.

X-ray Crystallography.

X-ray diffraction studies were carried out at the Caltech Division of Chemistry and Chemical Engineering X-ray Crystallography Facility using a dual-source Bruker D8 Venture, four-circle diffractometer with a PHOTON CMOS or a PHOTON II CPAD detector. Data were collected at 100 K using Mo Kα ($\lambda = 0.71073$ Å) or Cu Kα ($\lambda = 1.54178$ Å) radiation. The crystals were mounted on a glass fiber under paratone N oil. Structures were solved using SHELXT[45] and refined against F^2 on all data by full-matrix least squares with SHELXL.[46] All non-H atoms were refined anisotropically. All H atoms were placed at geometrically calculated positions and refined using a riding model. The isotropic displacement parameters of all H atoms were fixed at 1.2 (1.5 for methyl groups) times the U_{eq} value of the atoms to which they are bonded. Refinement details for individual structures are available in the SI.

Synthesis of [(P$_3$^B)Fe(NNMe$_2$)][BAr^F$_4$].

(P$_3$^B)Fe(NNMe$_2$) (25 mg, 0.036 mmol) was suspended in 1 mL of Et$_2$O in a 20 mL scintillation vial, which was subsequently charged with a magnetic stirbar and chilled to −78 °C in the cold well of a N$_2$-filled glovebox. A solution of [FeCp*$_2$][BAr^F$_4$] (43 mg, 0.036 mmol) in 4 mL of Et$_2$O was similarly chilled and then added dropwise to the stirring solution of (P$_3$^B)Fe(NNMe$_2$). After stirring for 30 min in the cold well, the resultant solution was allowed to warm to room temperature with stirring over 1 h, during which time a deep-orange-brown color developed. The solvent was then removed in vacuo, and the remaining solids washed with C$_6$H$_6$ (3 × 1 mL), then extracted with Et$_2$O (3 × 1 mL), and filtered. The filtrate was concentrated to ca. 1 mL, layered with pentane, and cooled to −35 °C. After 24 h, the mother liquor was decanted, and the remaining orange-red crystals were washed liberally with pentane and dried in vacuo to afford 49 mg of [(P$_3$^B)Fe(NNMe$_2$)][BAr^F$_4$] (87%). Recrystallization from 4:1 toluene/Et$_2$O at −35 °C yields material that is analytically pure except for the presence of cocrystallized toluene, which is not removed even under prolonged evacuation. NMR and elemental analysis indicate a [(P$_3$^B)Fe-(NNMe$_2$)][BAr^F$_4$]/toluene stoichiometry of 1:1. Crystals suitable for X-ray diffraction were obtained by layering an Et$_2$O solution of [(P^B$_3$)Fe(NNMe$_2$)][BAr^F$_4$] with pentane and cooling to −35 °C. ^{1}H NMR (500 MHz, THF-d$_8$, 293 K): δ 10.89 (v br), 7.79 (s, BAr^F$_4$ o-ArCH, 8H), 7.57 (s, BAr^F$_4$, p-ArCH, 4H), 2.22 (v br), −0.14 (v br). μ_{eff} (THF-d$_8$, Evans method, 293 K): 2.4 β_e (see the discussion of VT magnetization in the SI). UV−vis [THF, 293 K; λ, nm (ε, cm$^{−1}$ M$^{−1}$)]: ~270 (20720), 309 (12100), 407 (3024), 499 (734), 698 (106). Anal. Calcd for C$_{64}$H$_{58}$B$_2$F$_{24}$FeN$_2$P$_3$ + C$_7$H$_6$: C, 55.72; H, 4.86; N, 1.69. Found: C, 55.98; H, 4.67; N, 1.26.

Synthesis of [K(2-MeTHF)$_x$][(P$_3$^B)Fe(NNMe$_2$)].

A solution of (P$_3$^B)Fe(NNMe$_2$) in 2-MeTHF (5 to 10 mM) was chilled to −78 °C in the cold well of a N$_2$-filled glovebox. A vial containing 1.2 equiv of KC$_8$ and a magnetic stirbar was similarly chilled in the cold well. Using a prechilled glass pipet, the solution of (P$_3$^B)Fe(NNMe$_2$) was added to the vial containing solid KC$_8$ in a single shot, and this mixture was allowed to stir at −78 °C for 30 min. At this point, the procedure diverged, depending on the analysis. For X-band EPR measurements, this suspension was passed through a prechilled glass microfiber filter into a prechilled quartz X-band sample tube. A

similar procedure was used for the preparation of Q-band samples, but in order to prevent warming of the sample during transfer into the narrow Q-band sample tube, the suspension was filtered into a prechilled syringe equipped with a 22-gauge steel needle inserted into the tube. After the filtered solution had passed through the needle into the quartz tube, the syringe assembly was removed. For NRVS, the solution was filtered directly onto a prechilled copper sample holder. For Mössbauer analysis, the suspension was transferred into a prechilled delrin sample holder without filtration. At this point, in each of these cases, the cold well bath was replaced with liquid N_2, and the sample of $[(P_3^B)Fe(NNMe_2)]^-$ was frozen before being passed out of the glovebox and stored at 77 K prior to analysis.

Solutions of $[(P_3^B)Fe(NNMe_2)]^-$ are unstable upon warming, which has prevented its isolation in pure form. The decomposition kinetics are consistent with a unimolecular process (Figure S5), with a half-life at room temperature of approximately 4 min. Mössbauer analysis suggests that fresh preparations of $[(P_3^B)Fe(NNMe_2)]^-$ kept at $T \leq -78$ °C are typically ca. 75% pure. Because of this modest purity and the slow electronic relaxation of $[(P_3^B)Fe(NNMe_2)]^-$, NMR analysis was not conducted. Additional details on the growth of crystals of $[K(benzo-15-crown-5)_2][(P_3^B)Fe(NNMe_2)]$ suitable for X-ray diffraction are provided in the SI.

Supplementary Material

Refer to Web version on PubMed Central for supplementary material.

REFERENCES

(1). (a)Chatt J; Heath GA; Richards RL The reduction of ligating dinitrogen to yield a ligating N_2H_2 oiety. J. Chem. Soc., Chem. Commun 1972, 1010–1011.(b)Chatt J; Heath GA; Richards RL Diazene-N-(di-imide) and hydrazido-(2-)N-(aminoimido) complexes: the addition of acids to dinitrogen complexes. J. Chem. Soc., Dalton Trans 1974, 2074–2082.(c)Hidai M; Kodama T; Sato M; Harakawa M; Uchida Y Preparation and Properties of Dinitrogen- Molybdenum Complexes. 3. Preparation and Molecular Structure of 1-(η-Hydrazido(2-))fluorobis[1,2-bis(diphenylphosphino)ethane]-molybdenum Tetrafluoroborate-Dichloromethane Solvate, [Mo-$(N_2H_2)F(Ph_2PCH_2CH_2PPh_2)_2][BF_4]\cdot CH_2Cl_2$. Inorg. Chem 1976, 15, 2694–2697.(d)Chatt J; Hussain W; Leigh GJ; Neukomm H; Pickett CJ; Rankin DA The mechanism of the secondary alkylation of dinitrogen and the relationship between structure and reactivity in the alkylation of co-ordinated dinitrogen. J. Chem. Soc., Chem. Commun 1980, 1024–1025.

(2). (a)Chatt J; Dilworth JR; Richards RL Recent advances in the chemistry of nitrogen fixation. Chem. Rev 1978, 78, 589–625.(b)Dilworth JR Diazene, diazenido, isodiazene and hydrazido complexes. Coord. Chem. Rev 2017, 330, 53–94.

(3). (a)Hussain W; Leigh GJ; Pickett CJ Stepwise conversion of dinitrogen co-ordinated to molybdenum into an amine and an imido-complex. Relevance to the reactions of nitrogenase. J. Chem. Soc., Chem. Commun 1982, 747–748.(b)Horn KH; Böres N; Lehnert N; Mersmann K; Nather,ö C; Peters G; Tuczek F. Reduction Pathway of End-On Terminally Coordinated Dinitrogen. IV. Geometric, Electronic, and Vibrational Structure of a W(IV) Dialkylhydrazido Complex and Its Two-Electron-Reduced Derivative Undergoing N-N Cleavage upon Protonation. Inorg. Chem 2005, 44, 3016–3030. [PubMed: 15847406] (c)Dreher A; Mersmann K; Nather C; Ivanovic-Burmazovic I; van Eldik R; Tuczek F. Structural, Spectroscopic, and Kinetic Investigation of the Molybdenum Dialkylhydrazido Complexes [MoBr(NNC_5H_{10})-(dppe)_2]Br and [Mo(NNC_5H_{10})(dppe)_2]: Activation Parameters and Revised Mechanism for N-N Cleavage. Inorg. Chem 2009, 48, 2078–2093. [PubMed: 19235969] (d)Patel S; Li Y; Odom AL Synthesis, Structure, and LLCT Transitions in Terminal Hydrazido(2-) Bipyridine Complexes of Titanium. Inorg. Chem 2007, 46, 6373–6381. [PubMed: 17625836] (e)Keane AJ; Zavalij PY; Sita LR N-N

Bond Cleavage of Mid-Valent Ta(IV) Hydrazido and Hydrazidium Complexes Relevant to the Schrock Cycle for Dinitrogen Fixation. J. Am. Chem. Soc 2013, 135, 9580–9583. [PubMed: 23725566]

(4). Pearce AJ; Cassabaum AA; Gast GE; Frontiera RR; Tonks IA Redox Non-Innocent Behavior of a Terminal Iridium Hydrazido(2-) Triple Bond. Angew. Chem., Int. Ed 2016, 55, 13169–13173.

(5). Stucke N; Floser BM; Weyrich T; Tuczek F Nitrogen Fixation Catalyzed by Transition Metal Complexes: Recent Developments. Eur. J. Inorg. Chem 2018, 2018, 1337–1355.

(6). (a)Mansuy D; Battioni P; Mahy JP Isolation of an Iron- Nitrene Complex from the Dioxygen and Iron Porphyrin Dependent Oxidation of a Hydrazine. J. Am. Chem. Soc 1982, 104, 4487–4489. (b)Mahy JP; Battioni P; Mansuy D; Fisher J; Weiss R; Mispelter J; Morgenstern-Badarau I; Gans P Iron Porphyrin-Nitrene Complexes: Preparation from 1,1-Dialkylhydrazines. Electronic Structure from NMR, Mössbauer, and Magnetic Susceptibility Studies and Crystal Structure of the [Tetrakis(p-chlorophenyl)porphyrinato]-[(2,2,6,6-tetramethyl-1-piperidyl)nitrene]iron Complex. J. Am. Chem. Soc 1984, 106, 1699–1706.(c)Moret M-E; Peters JC N_2 Functionalization at Iron Metallaboratranes. J. Am. Chem. Soc 2011, 133, 18118–18121. [PubMed: 22008018] (d)Suess DLM; Peters JC H-H and Si-H Bond Addition to Fe≡NNR$_2$ Intermediates Derived from N_2. J. Am. Chem. Soc 2013, 135, 4938–4941. [PubMed: 23472709] (e)Rudd PA; Planas N; Bill E; Gagliardi L; Lu CC Dinitrogen Activation at Iron and Cobalt Metallalumatranes. Eur. J. Inorg. Chem 2013, 2013, 3898–3906.(f)McWilliams SF; Bill E; Lukat-Rodgers G; Rodgers KR; Mercado BQ; Holland PL Effects of N_2 Binding Mode on Iron-Based Functionalization of Dinitrogen to Form an Iron(III) Hydrazido Complex. J. Am. Chem. Soc 2018, 140, 8586–8598. [PubMed: 29957940]

(7). Anderson JS; Cutsail GE; Rittle J; Connor BA; Gunderson WA; Zhang L; Hoffman BM; Peters JC Characterization of an Fe≡N-NH$_2$ Intermediate Relevant to Catalytic N_2 Reduction to NH$_3$. J. Am. Chem. Soc 2015, 137, 7803–7809. [PubMed: 26000443]

(8). Thompson NB; Green MT; Peters JC Nitrogen Fixation via a Terminal Fe(IV) Nitride. J. Am. Chem. Soc 2017, 139, 15312–15315. [PubMed: 28992418]

(9). Rittle J; Peters JC An Fe-N$_2$ Complex That Generates Hydrazine and Ammonia via Fe≡NNH$_2$: Demonstrating a Hybrid Distal-to-Alternating Pathway for N_2 Reduction. J. Am. Chem. Soc 2016, 138, 4243–4248. [PubMed: 26937584]

(10). (a)Suarez AIO; Lyaskovskyy V; Reek JNH; van der Vlugt JI; de Bruin B Complexes with Nitrogen-Centered Radical Ligands: Classification, Spectroscopic Features, Reactivity, and Catalytic Applications. Angew. Chem., Int. Ed 2013, 52, 12510–12529.(b)Kogut E; Wiencko HL; Zhang L; Cordeau DE; Warren TH A Terminal Ni(III)-Imide with Diverse Reactivity Pathways. J. Am. Chem. Soc 2005, 127, 11248–11249. [PubMed: 16089446] (c)Mankad NP; Antholine WE; Szilagyi RK; Peters JC Three-Coordinate Copper(I) Amido and Aminyl Radical Complexes. J. Am. Chem. Soc 2009, 131, 3878–3880. [PubMed: 19253942] (d)Cowley RE; Eckert NA; Vaddadi S; Figg TM; Cundari TR; Holland PL Selectivity and Mechanism of Hydrogen Atom Transfer by an Isolable Imidoiron(III) Complex. J. Am. Chem. Soc 2011, 133, 9796–9811. [PubMed: 21563763] (e)King ER; Hennessy ET; Betley TA Catalytic C-H Bond Amination from High-Spin Iron Imido Complexes. J. Am. Chem. Soc 2011, 133, 4917–4923. [PubMed: 21405138] (f)Iovan DA; Betley TA Characterization of Iron-Imido Species Relevant for N-Group Transfer Chemistry. J. Am. Chem. Soc 2016, 138, 1983–1993. [PubMed: 26788747]

(11). Del Castillo TJ; Thompson NB; Peters JC A Synthetic Single-Site Fe Nitrogenase: High Turnover, Freeze-Quench 57Fe Mössbauer Data, and a Hydride Resting State. J. Am. Chem. Soc 2016, 138, 5341–5350. [PubMed: 27026402]

(12). (a)Chalkley MJ; Del Castillo TJ; Matson BD; Roddy JP; Peters JC Catalytic N_2-to-NH$_3$ Conversion by Fe at Lower Driving Force: A Proposed Role for Metallocene-Mediated PCET. ACS Cent. Sci 2017, 3, 217–223. [PubMed: 28386599] (b)Matson BD; Peters JC Fe-Mediated HER vs N_2RR: Exploring Factors That Contribute to Selectivity in P3EFe(N_2) (E = B, Si, C) Catalyst Model Systems. ACS Catal 2018, 8, 1448–1455. [PubMed: 30555733] (c)Chalkley MJ; Del Castillo TJ; Matson BD; Peters JC Fe-Mediated Nitrogen Fixation with a Metallocene Mediator: Exploring pK$_a$ Effects and Demonstrating Electrocatalysis. J. Am. Chem. Soc 2018, 140, 6122–6129. [PubMed: 29669205]

(13). (a)Kahlal S; Saillard J-Y; Hamon J-R; Manzur C; Carrillo D Molecular orbital analysis of the metal-hydrazide(2-) bonding in co-ordination chemistry. J. Chem. Soc., Dalton Trans 1998,

1229–1240.(b)Kahlal S; Saillard J-Y; Hamon J-R; Manzur C; Carrillo D Bonding analysis of transition metal NNR end-on complexes and comparison with isoelectronic NNR_2 species. New J. Chem 2001, 25, 231–242.

(14). (a)Hinsberg WD; Dervan PB Synthesis and Direct Spectroscopic Observation of a 1,1-Dialkyldiazene. Infrared and Electronic Spectrum of N-(2,2,6,6-tetramethylpiperidyl)nitrene. J. Am. Chem. Soc 1978, 100, 1608–1610.(b)Sylwester AP; Dervan PB Low-Temperature Matrix Isolation of H_2NN. Electronic and Infrared Characterization. J. Am. Chem. Soc 1984, 106, 4648–4650.(c)Stepanic V; Baranovic G. Ground and excited states of isodiazene - an ab initio study. Chem. Phys 2000, 254, 151–168.

(15). Speelman AL; Lehnert N Heme versus Non-Heme Iron-Nitroxyl $\{FeN(H)O\}^8$ Complexes: Electronic Structure and Biologically Relevant Reactivity. Acc. Chem. Res 2014, 47, 1106–1116. [PubMed: 24555413]

(16). (a)Malatesta V; Ingold KU Electron paramagnetic resonance spectra of 1,1-dialkylhydrazyl radicals in solution. J. Am. Chem. Soc 1973, 95, 6110–6113.(b)Malatesta V; Lindsay D; Horswill EC; Ingold KU The EPR Spectra of Hydrazyl and Some 1-Substituted Hydrazyl Radicals in Solution. Can. J. Chem 1974, 52, 864–866.(c)Smith P; Stevens RD; Kaba RA Electron paramagnetic resonance spectroscopic study of radical cations from hydrazine, methylhydrazine, and dimethylhydrazines. J. Phys. Chem 1971, 75, 2048–2055.

(17). Vela J; Cirera J; Smith JM; Lachicotte RJ; Flaschenriem CJ; Alvarez S; Holland PL Quantitative Geometric Descriptions of the Belt Iron Atoms of the Iron-Molybdenum Cofactor of Nitrogenase and Synthetic Iron(II) Model Complexes. Inorg. Chem 2007, 46, 60–71. [PubMed: 17198413]

(18). Pasinszki T; Krebsz M; Tarczay G; Wentrup C Photolysis of Dimethylcarbamoyl Azide in an Argon Matrix: Spectroscopic Identification of Dimethylamino Isocyanate and 1,1-Dimethyldiazene.J. Org. Chem 2013, 78, 11985–11991. [PubMed: 24191697]

(19). Cotton FA; Wilkinson G Advanced Inorganic Chemistry, 5th ed.; Wiley: New York, 1988.

(20). (a)Galindo A; Hills A; Hughes DL; Richards RL A complex of the hydrazidium (=N-NH +3) ligand: X-ray structure of $[WCl(NNH_3)(PMe_3)_4]Cl_2$. J. Chem. Soc., Chem. Commun 1987, 1815–1816.(b)Galindo A; Hills A; Hughes DL; Richards RL; Hughes M; Mason J Protonation reactions of dinitrogen complexes of molybdenum and tungsten with PMe_3 as Co-ligand. X-Ray structure of the hydrazidium complex $[WCl(NNH_3)(PMe_3)_4]Cl_2$. J. Chem. Soc., Dalton Trans 1990, 283–288.(c)Vale MG; Schrock RR Synthesis and Reactions of Monomeric Hydrazine and Hydrazido Complexes that Contain the $Cp*MoMe_3$ Core. Inorg. Chem 1993, 32, 2767–2772. (d)Li Y; Shi Y; Odom AL Titanium Hydrazido and Imido Complexes: Synthesis, Structure, Reactivity, and Relevance to Alkyne Hydroamination. J. Am. Chem. Soc 2004, 126, 1794–1803. [PubMed: 14871111] (e)Clulow AJ; Selby JD; Cushion MG; Schwarz AD; Mountford P Synthesis, Structures and Reactivity of Group 4 Hydrazido Complexes Supported by Calix[4]arene Ligands. Inorg. Chem 2008, 47, 12049– 12062. [PubMed: 18998672] (f)Tiong PJ; Nova A; Schwarz AD; Selby JD; Clot E; Mountford P Site selectivity and reversibility in the reactions of titanium hydrazides with Si-H, Si-X, C-X and H^+ reagents: $Ti=N_\alpha$ 1,2-silane addition, N_β alkylation, N_α protonation and σ-bond metathesis. Dalton Trans 2012, 41, 2277–2288. [PubMed: 22223159]

(21). Groom CR; Bruno IJ; Lightfoot MP; Ward SC The Cambridge Structural Database. Acta Crystallogr., Sect. B: Struct. Sci., Cryst. Eng. Mater 2016, 72, 171–179.

(22). (a)Rohde J-U; Betley TA; Jackson TA; Saouma CT; Peters JC; Que L XAS Characterization of a Nitridoiron(IV) Complex with a Very Short Fe-N Bond. Inorg. Chem 2007, 46, 5720–5726. [PubMed: 17569533] (b)Vogel C; Heinemann FW; Sutter J; Anthon C; Meyer K An Iron Nitride Complex. Angew. Chem., Int. Ed 2008, 47, 2681–2684.(c)Scepaniak JJ; Fulton MD; Bontchev RP; Duesler EN; Kirk ML; Smith JM Structural and Spectroscopic Characterization of an Electrophilic Iron Nitrido Complex. J. Am. Chem. Soc 2008, 130, 10515–10517. [PubMed: 18630913]

(23). Gütlich P; Bill E; Trautwein AX Mössbauer Spectroscopy and Transition Metal Chemistry: Fundamentals and Applications; Springer: New York, 2011.

(24). (a)Praneeth VKK; Nather C; Peters G; Lehnert N. Spectroscopic Properties and Electronic Structure of Five-and Six-Coordinate Iron(II) Porphyrin NO Complexes: Effect of the Axial N-Donor Ligand. Inorg. Chem 2006, 45, 2795–2811. [PubMed: 16562937] (b)Paulat F; Berto TC;

DeBeer George S; Goodrich L; Praneeth VKK; Sulok CD; Lehnert N Vibrational Assignments of Six-Coordinate Ferrous Heme Nitrosyls: New Insight from Nuclear Resonance Vibrational Spectroscopy. Inorg. Chem 2008, 47, 11449–11451. [PubMed: 18998631]

(25). Morton JR; Preston KF Atomic parameters for paramagnetic resonance data. J. Magn. Reson 1978, 30, 577–582.

(26). Moret ME; Peters JC Terminal Iron Dinitrogen and Iron Imide Complexes Supported by a Tris(phosphino)borane Ligand. Angew. Chem., Int. Ed 2011, 50, 2063–2067.

(27). Dykstra CE; Schaefer HF Excited electronic states of ketene.J. Am. Chem. Soc 1976, 98, 2689–2695.

(28). (a)Shoji M; Nishiyama Y; Maruno Y; Koizumi K; Kitagawa Y; Yamanaka S; Kawakami T; Okumura M; Yamaguchi K Theory of chemical bonds in metalloenzymes I: Analytical and hybrid-DFT studies on oxo and hydroxo diiron cores. Int. J. Quantum Chem 2004, 100, 887–906. (b)Pierloot K; Zhao H; Vancoillie S Copper Corroles: the Question of Noninnocence. Inorg. Chem 2010, 49, 10316–10329. [PubMed: 20964313] (c)Radon M; Broclawik E; Pierloot K Electronic Structure of Selected {FeNO}^{7} Complexes in Heme and Non-Heme Architectures: A Density Functional and Multireference ab Initio Study. J. Phys. Chem. B 2010, 114, 1518–1528. [PubMed: 20047294] (d)Tomson NC; Crimmin MR; Petrenko T; Rosebrugh LE; Sproules S; Boyd WC; Bergman RG; DeBeer S; Toste FD; Wieghardt K A Step beyond the Feltham-Enemark Notation: Spectroscopic and Correlated ab Initio Computational Support for an Antiferromagnetically Coupled M(II)-(NO)⁻ Description of Tp*M(NO) (M = Co, Ni). J. Am. Chem. Soc 2011, 133, 18785–18801. [PubMed: 22047035]

(29). Speelman AL; Zhang B; Krebs C; Lehnert N Structural and Spectroscopic Characterization of a High-Spin {FeNO}^{6} Complex with an Iron(IV)-NO⁻ Electronic Structure. Angew. Chem., Int. Ed 2016, 55, 6685–6688.

(30). Ye S; Geng C-Y; Shaik S; Neese F Electronic structure analysis of multistate reactivity in transition metal catalyzed reactions: the case of C-H bond activation by non-heme iron(IV)-oxo cores. Phys. Chem. Chem. Phys 2013, 15, 8017–8030. [PubMed: 23632340]

(31). Jensen HJA; Joergensen P; Helgaker T Ground-state potential energy surface of diazene. J. Am. Chem. Soc 1987, 109, 2895–2901.

(32). Lehnert N; Wiesler BE; Tuczek F; Hennige A; Sellmann D Activation of Diazene and the Nitrogenase Problem: An Investigation of Diazene-Bridged Fe(II) Centers with Sulfur Ligand Sphere. 2. Vibrational Properties. J. Am. Chem. Soc 1997, 119, 8879–8888.

(33). Lehnert N; Tuczek F The Reduction Pathway of End-on Coordinated Dinitrogen. I. Vibrational Spectra of Mo/W-N$_2$, - NNH, and - NNH$_2$ Complexes and Quantum Chemistry Assisted Normal Coordinate Analysis. Inorg. Chem 1999, 38, 1659–1670. [PubMed: 11670933]

(34). Horn KH; Lehnert N; Tuczek F Reduction Pathway of End-On Coordinated Dinitrogen. 3. Electronic Structure and Spectroscopic Properties of Molybdenum/Tungsten Hydrazidium Complexes. Inorg. Chem 2003, 42, 1076–1086. [PubMed: 12588141]

(35). Fessenden RW Electron spin resonance spectra of some isotopically substituted hydrocarbon radicals. J. Phys. Chem 1967, 71, 74–83.

(36). Lu J-B; Ma X-L; Wang J-Q; Liu J-C; Xiao H; Li J Efficient Nitrogen Fixation via a Redox-Flexible Single-Iron Site with Reverse-Dative Iron → Boron σ Bonding. J. Phys. Chem. A 2018, 122, 4530–4537. [PubMed: 29648830]

(37). Del Castillo TJ; Thompson NB; Suess DLM; Ung G; Peters JC Evaluating Molecular Cobalt Complexes for the Conversion of N$_2$ to NH$_3$. Inorg. Chem 2015, 54, 9256–9262. [PubMed: 26001022]

(38). Rittle J; Peters JC N-H Bond Dissociation Enthalpies and Facile H Atom Transfers for Early Intermediates of Fe-N$_2$ and Fe-CN Reductions. J. Am. Chem. Soc 2017, 139, 3161–3170. [PubMed: 28140600]

(39). Yandulov DV; Schrock RR Studies Relevant to Catalytic Reduction of Dinitrogen to Ammonia by Molybdenum Triamidoamine Complexes. Inorg. Chem 2005, 44, 1103–1117. [PubMed: 15859292]

(40). Mersmann K; Horn KH; Böres N; Lehnert N; Studt F; Paulat F; Peters G; Ivanovic-Burmazovic I; van Eldik R; Tuczek F Reduction Pathway of End-On Terminally Coordinated Dinitrogen. V.

N-N Bond Cleavage in Mo/W Hydrazidium Complexes with Diphosphine Coligands. Comparison with Triamidoamine Systems. Inorg. Chem 2005, 44, 3031–3045. [PubMed: 15847407]

(41). Sippel D; Rohde M; Netzer J; Trncik C; Gies J; Grunau K; Djurdjevic I; Decamps L; Andrade SLA; Einsle O A bound reaction intermediate sheds light on the mechanism of nitrogenase. Science 2018, 359, 1484. [PubMed: 29599235]

(42). Prisecaru I WMOSS4 Mössbauer Spectral Analysis Software; www.wmoss.org, 2009–2016.

(43). Lehnert N; Galinato MGI; Paulat F; Richter-Addo GB; Sturhahn W; Xu N; Zhao J Nuclear Resonance Vibrational Spectroscopy Applied to [Fe(OEP)(NO)]: The Vibrational Assignments of Five-Coordinate Ferrous Heme-Nitrosyls and Implications for Electronic Structure. Inorg. Chem 2010, 49, 4133–4148. [PubMed: 20345089]

(44). (a)Sage JT; Paxson C; Wyllie GRA; Sturhahn W; Durbin SM; Champion PM; Alp EE; Scheidt WR Nuclear resonance vibrational spectroscopy of a protein active-site mimic. J. Phys.: Condens. Matter 2001, 13, 7707–7722.(b)Sturhahn W Nuclear resonant spectroscopy. J. Phys.: Condens. Matter 2004, 16, S497–S530.

(45). Sheldrick G SHELXT-Integrated space-group and crystal-structure determination. Acta Crystallogr., Sect. A: Found. Adv 2015, 71, 3–8. [PubMed: 25537383]

(46). Sheldrick G Crystal structure refinement with SHELXL. Acta Crystallogr., Sect. C: Struct. Chem 2015, 71, 3–8. [PubMed: 25567568]
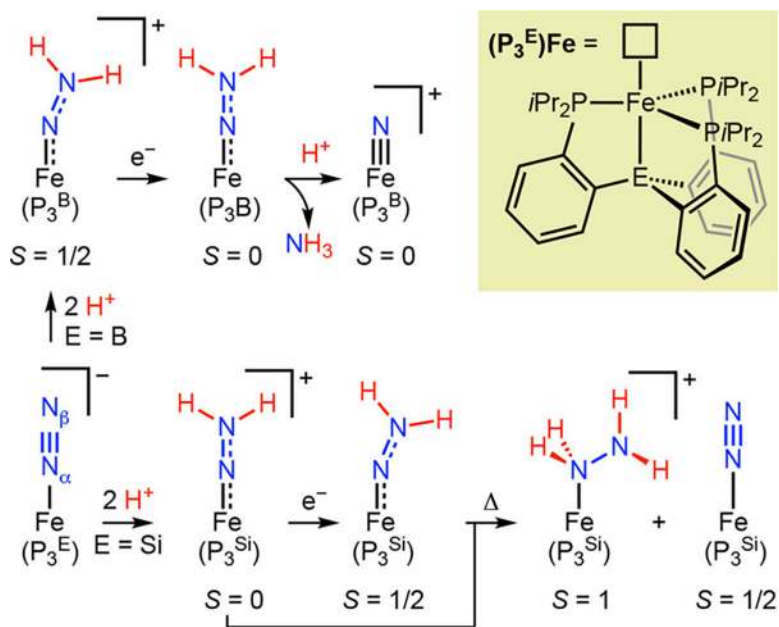
Figure 1.
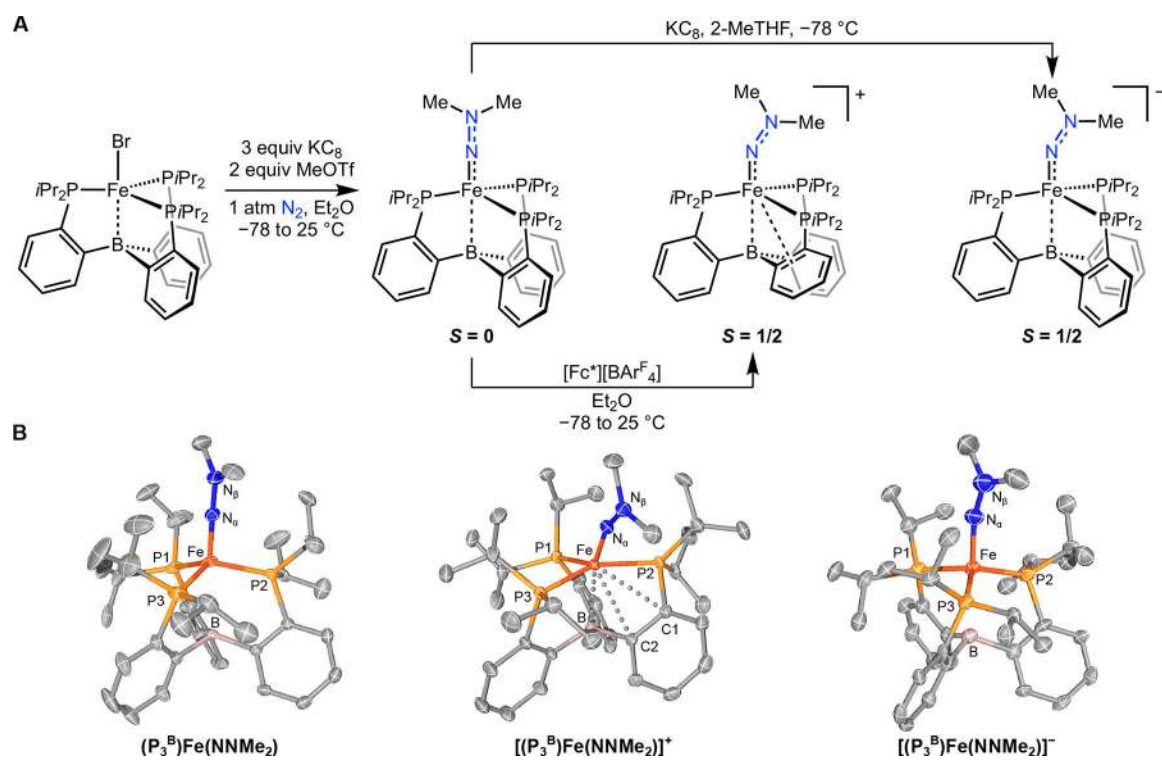Observed reactivity of $(P_3^E)Fe(NNH_2)$ complexes.

Figure 2.
Synthesis (A) and solid-state structures (B) of the $[(P_3^B)Fe(NNMe_2)]^{+/0/-}$ redox series. Ellipsoids are shown at 50% probability, with H atoms and counterions omitted for clarity.
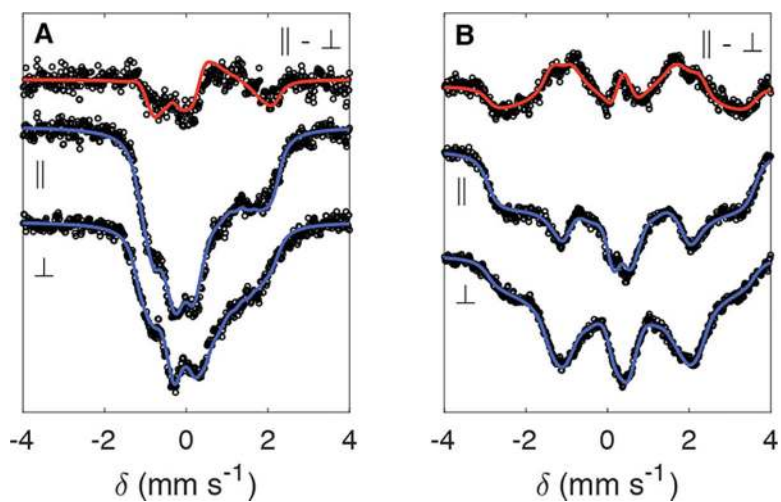
Figure 3.
Frozen-solution Mössbauer spectra collected at 80 K in the presence of a 50 mT external field, oriented parallel or perpendicular to the γ-rays, as indicated. Data are shown as open circles, with simulations in blue; the field-orientation difference spectra are shown at the top, with the simulated difference spectrum in red. (A) Spectra of $[(P_3^B)Fe(NNMe_2)]^+$. (B) Spectra of $[(P_3^B)Fe(NNMe_2)]^-$. For clarity, minor quadrupole doublet impurities have been subtracted from the spectra in part B.
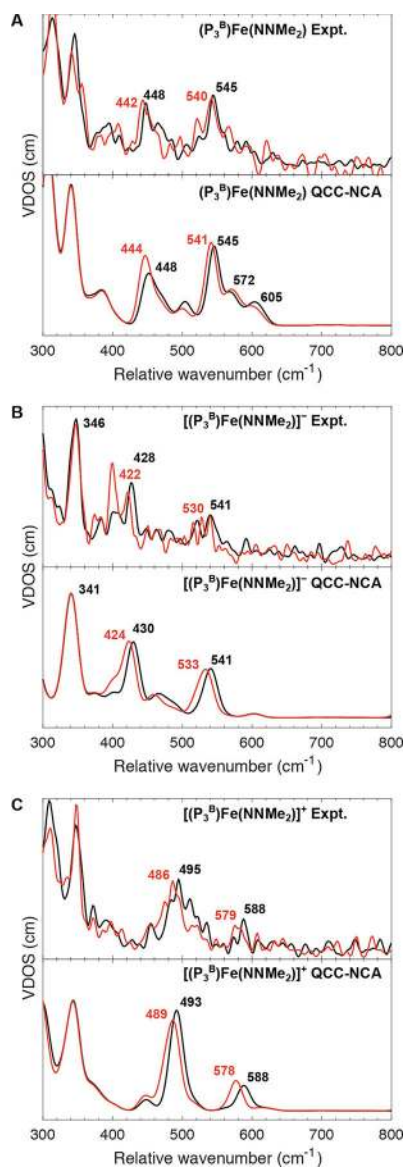
Figure 4.
Experimental NRVS VDOS (top) and QCC-NCA fit (bottom) for $[(P_3{}^B){}^{57}Fe({}^{14}N{}^{14}NMe_2)]^n$ (black) and $[(P_3{}^B){}^{57}Fe\text{-}({}^{15}N{}^{15}NMe_2)]^n$ (red). (A) Neutral complex. (B) Anionic complex.(C) Cationic complex.
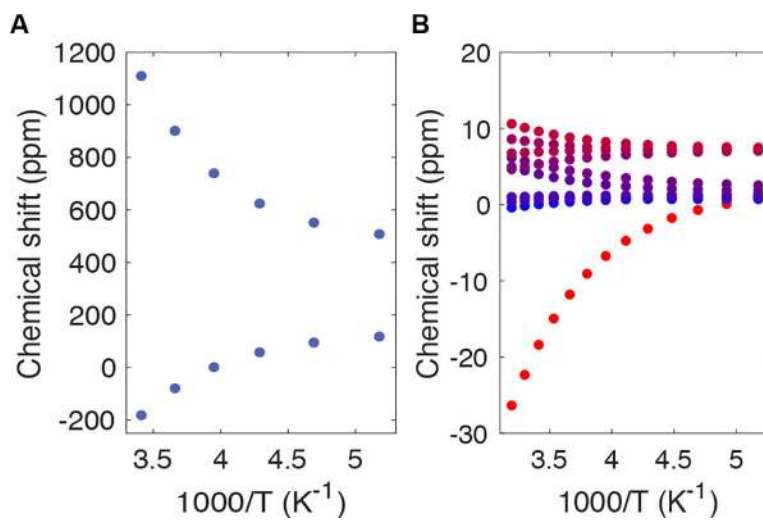
Figure 5.
(A) VT ^{15}N NMR for $(P_3{}^B)Fe(^{15}N^{15}NMe_2)$. (B) VT ^1H NMR for $(P_3{}^B)Fe(NNMe_2)$. The resonance due to the $N-CH_3$ protons is plotted in bright red.
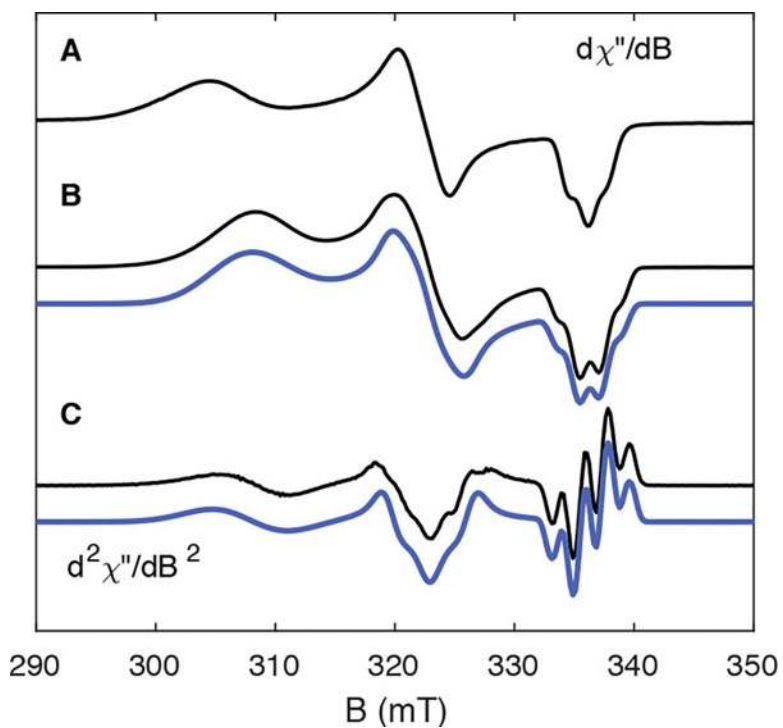
Figure 6.
(A) CW X-band EPR spectrum of $[(P_3^B)Fe(NNH_2)]^+$. A full simulation can be found in ref 7. (B) CW X-band EPR spectrum of $[(P_3^B)Fe(NNMe_2)]^+$. Data are plotted in black with a simulation in blue. (C) Second-derivative spectra of those presented in part B. All data were collected at 77 K with a power of 2 mW.
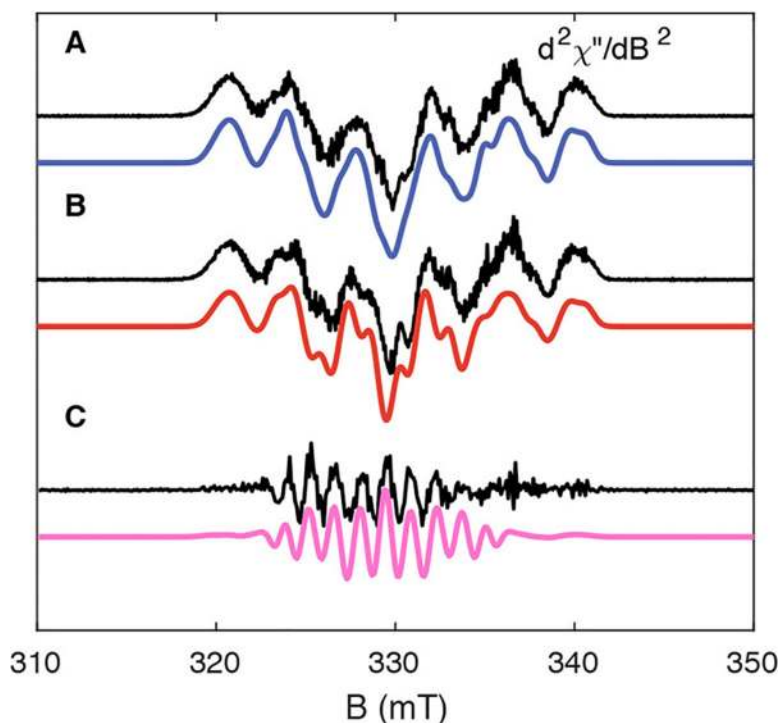
Figure 7.
(A) CW X-band EPR spectrum (second derivative) of $[(P_3^B)Fe(^{14}N^{14}NMe_2)]^-$. Data are plotted in black with a simulation in blue. (B) CW X-band EPR spectrum (second derivative) of $[(P_3^B)Fe(^{15}N^{15}NMe_2)]^-$. Data are plotted in black with a simulation in red. (C) Difference spectrum for the data shown in parts A and B. Data are plotted in black with a difference of the simulations in pink. All data were collected at 77 K with a power of 0.2 mW.
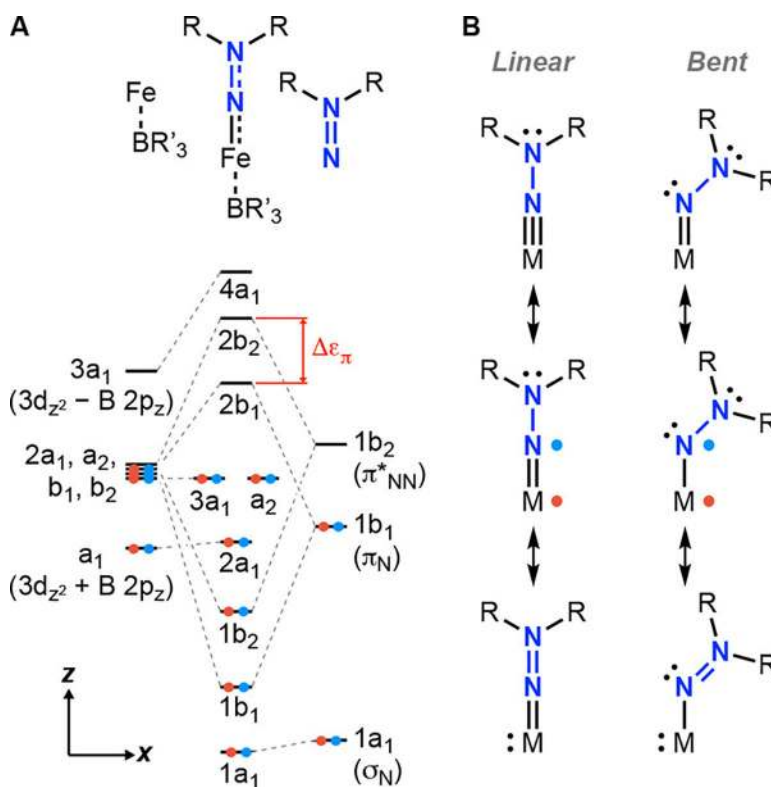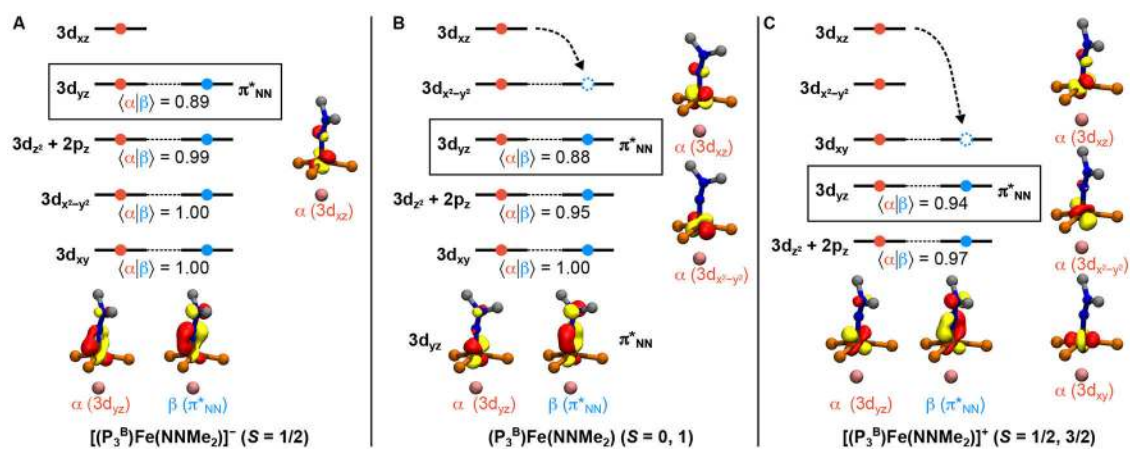
Figure 8.
(A) Qualitative MO diagram for $R'_3B-Fe-NNH_2$ under pseudo-C_{2v} symmetry. (B) VB diagrams describing possible resonance structures of a $M-NNR_2$ moiety, including covalent and antiferromagnetic representations. Red dots indicate α-spin electrons, while blue dots indicate β-spin electrons.

Figure 9.
Magnetic orbitals (isovalue = 0.075 au) and qualitative MO diagrams from BS DFT calculations (TPSSh) of (A) $[(P_3^B)Fe(NNMe_2)]^-$, (B) $(P_3^B)Fe(NNMe_2)$ in its triplet excited state, and (C) $[(P_3^B)Fe(NNMe_2)]^+$ in its quartet excited state. For parts B and C, the dashed arrow indicates relaxation to the ground-state configurations suggested by DFT calculations, in which $\langle \alpha | \beta \rangle \rightarrow 1$ for all corresponding orbitals.
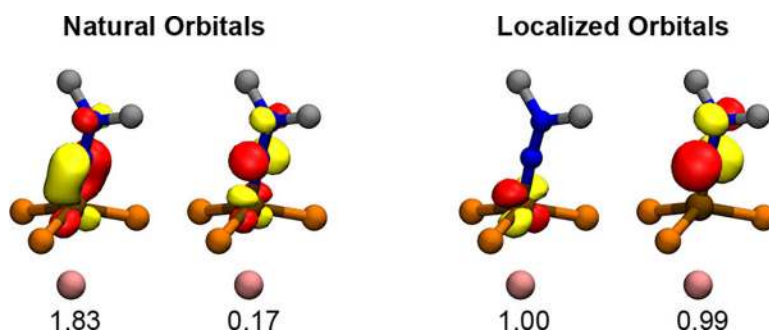
Figure 10.
Active space orbitals (isovalue = 0.075 au) corresponding to the Fe−NNMe$_2$ out-of-plane π interactions from a ground-state-specific CASSCF calculation of (P$_3$^{B})Fe(NNMe$_2$). Natural and localized orbital bases are presented along with occupation numbers.
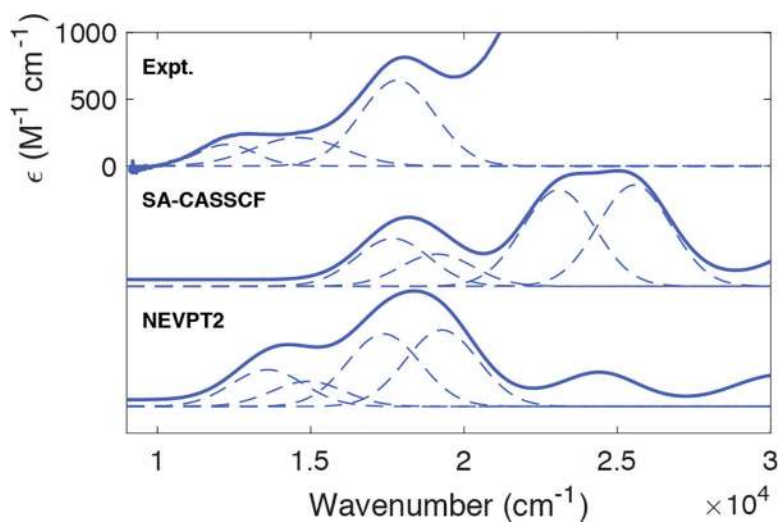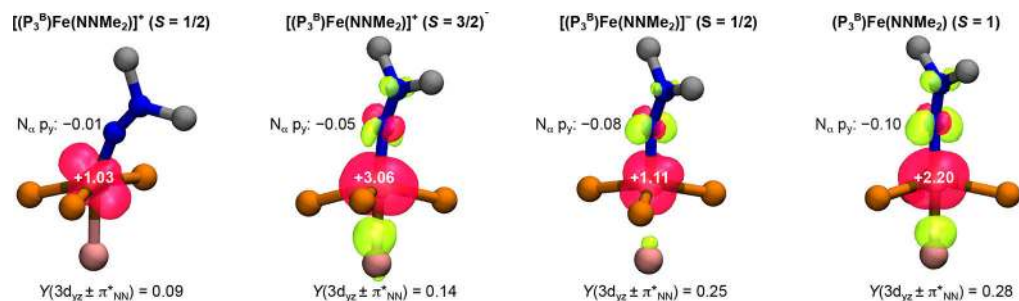
Figure 11.
Experimental and ab initio electronic spectra of $(P_3{}^B)Fe-(NNMe_2)$. The experimental spectrum was collected in 2-MeTHF at 153 K. A Gaussian spectral deconvolution is shown for the lowest three or four singlet excited states.

Figure 12.
Spin-density isosurfaces (isovalue = 0.005 au) from CASSCF calculations. The α density is shown in red, while the β density is shown in green. Selected Löwdin spin populations are given, along with the diradical index (Y) given in Table 5.
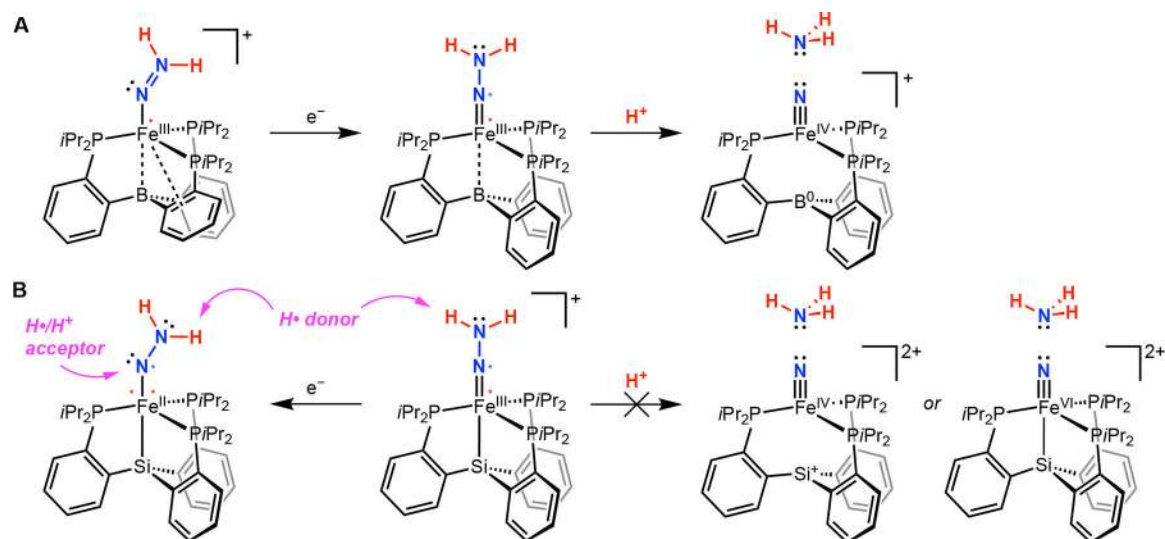
Figure 13.
(A) Proposed mechanism of N−N bond cleavage by $[(P_3^B)Fe(NNH_2)]^+$. (B) Proposed role of ligand radical character in the N−H bond-forming reactivity of $[(P_3^{Si})Fe(NNH_2)]^{+/0}$. Formal Fe oxidation states are given assuming a covalent Fe−E interaction; however, see the discussion in section 3.2

Table 1.

Collected ^{57}Fe Mössbauer Parameters[a]

complex	δ (mm s^{-1})	$|\Delta E_Q|$ (mms^{-1})	a$_{iso}$ (MHz)[b]
[(P$_3$^{B})Fe(NNMe$_2$)]$^+$	0.31 [0.35(4)]	1.16 [0.6(3)]	11.8 [7.4]
[(P$_3$^{B})Fe(NNH$_2$)]$^{+c}$	0.35	1.02	n.d.
(P$_3$^{B})Fe(NNMe$_2$)^d	0.17	1.73	
(P3^B)Fe(NNH$_2$)^d	0.14	1.63	
(P$_3$^{B})Fe(NN[Si$_2$])	0.19	1.85	
[(P$_3$^{Si})Fe(NNH$_2$)]$^{+e}$	0.13	1.48	
[(P$_3$^{Si})Fe(NNMe$_2$)]$^{+e}$	0.14	1.49	
(P$_3$^{B})Fe(NAd)^f	0.04	1.40	
[(P$_3$^{B})Fe(NNMe$_2$)]$^-$	0.39 [0.41(4)]	1.20 [1.1(3)]	29.1 [−20.7]
(P$_3$^{Si})Fe(NNH$_2$)^e	0.31	0.86	25.4
(P$_3$^{Si})Fe(NNMe$_2$)^e	0.36	0.90	26.5

[a]DFT-calculated values are given in square brackets.

[b]The isotropic ^{57}Fe HFC constant (sign not determined). Full simulation parameters for magnetically perturbed spectra can be found in the SI.

[c]From ref 7.

[d]From ref 8.

[e]From ref 9.

[f]From ref 11.

Table 2.

Summary of Key Force Constants from QCC-NCA[a]

complex	Fe-N	N-N	Fe-N-N$_{IP}$[b]
$[(P_3^B)Fe(NNMe_2)]^+$	3.59	8.55	0.59
$(P_3^B)Fe(NNMe_2)$	4.83	6.83	1.98
$[(P_3^B)Fe(NNMe_2)]^-$	2.97	6.78	0.68

[a]Force constants are in units of mdyn Å^{-1} for stretches and in units of mdyn Å for bends.

[b]The in-plane bending force constant.

Table 3.

Collected g Tensors

complex	g_1	g_2	g_3	g_{iso}	Δg[a]
$[(P_3{}^B)Fe(NNMe_2)]^+$	2.005	2.089	2.192	2.095	0.187
$[(P_3{}^B)Fe(NNH_2)]^{+}$[b]	2.006	2.091	2.222	2.106	0.216
$[(P_3{}^B)Fe(NAd)]^+$	1.970	2.058	2.419	2.149	0.449
$[(P_3{}^B)Fe(NNMe_2)]^-$	2.006	2.041	2.068	2.038	0.062
$(P_3{}^{Si})Fe(NNH_2)$[c]	2.004	2.027	2.070	2.034	0.066
$(P_3{}^{Si})Fe(NNMe_2)$[c]	2.000	2.030	2.080	2.037	0.080

[a]$\Delta g = g3 - g1$.

[b]From ref 7.

[c]From ref 9.

Table 4.

Collected HFC Constants of $[(P_3{}^B)Fe(NNMe_2)]^n$

n	nucleus	A_1 (MHz)[a]	A_2 (MHz)[a]	A_3 (MHz)[a]	a_{iso} (MHz)
+	$^{14}N_{\alpha4}$[b]	−10.7	−5.7	−0.1	−5.7
+	$^{14}N_{\beta}$[b]	−1.5	−7.3	−1.5	−3.4
+	N-Me $^{13}C_{\alpha}$	9.7	8.5	11.0	9.7
+	N-Me $^{13}C_{\beta}$	8.4	6.7	8.8	8.0
+	$^{31}P_{\alpha}$	48.5	73.0	51.7	57.7
+	$^{31}P_{\beta}$	55.2	49.0	36.5	46.9
+	$^{31}P_{\gamma}$	40.0	30.0	36.5	35.5
+	^{11}B	10.3	9.6	7.6	9.2
−	$^{14}N_{\alpha}$[b]	−3.9	−29.2	11.8	−7.1
−	$^{14}N_{\beta}$[b]	1.6	−5.7	1.6	−0.9
−	N-Me ^{13}C	20.0	20.9	18.0	19.6
−	$^{31}P_{\alpha}$	134.6	124.6	116.6	125.3
−	$^{31}P_{\beta}$	82.9	82.6	79.3	81.6
−	$^{31}P_{\gamma}$	28.1	30.0	27.6	28.6
−	^{11}B	15.9	15.2	14.7	15.3

[a] With the exception of N_{α} for the cationic complex (see the SI), the HFC tensors are taken to be coincident with the g frame, with $g_1 = g_{min}$, $g_2 = g_{mid}$, and $g_3 = g_{max}$.

[b] The absolute signs of A have not been determined experimentally but are assigned to be consistent with prior ENDOR studies and calculations (see ref 7).

Table 5.

Diradical Character and Population Analysis of the $3d_{yz}/\pi^*_{NN}$ Interaction from CASSCF

complex	S	Y^a ($3d_{yz} \pm \pi^*_{NN}$)	$3d_{yz} + \pi^*_{NN}{}^b$	
			% Fe	% $N_\alpha + N_\beta$
$[(P_3{}^B)Fe(NNMe_2)]^+$	½	0.09	68.9	9.7
	$^3/_2$	0.14	71.3	11.8
$(P_3{}^B)Fe(NNMe_2)$	0	0.17	48.9	27
	1	0.28	56.0	24.9
$[(P_3{}^B)Fe(NNMe_2)]^-$	½	0.2S	49.1	19

^{a}Y = 1 - (n$_+$ - n$_-$)/2.

^{b}Löwdin population analysis.

Table 6.

Prediction of g Tensors and Anisotropic ^{14}N HFC Tensors from Theory

parameter	$[(P_3{}^B)Fe(NNMe_2)]^+$		$[(P_3{}^B)Fe(NNMe_2)]^-$	
	expt	CASSCF	expt	CASSCF
$\Delta g_1{}^a$	2.7	1.8	3.7	−1.5
$\Delta g_2{}^a$	87	113	39	35
$\Delta g_3{}^a$	190	246	66	54
$t(^{14}N_a)$ (MHz)	−2.5	−1.4	−11.1	−8.0
$t(^{14}N_\beta)$ (MHz)	−1.9	−0.6	−2.4	−1.8
$\delta_{HFC}(^{14}N_a)$	~1	0.5	0.7	0.6
$\delta_{HFC}(^{14}N_\beta)$	~0	0.6	~0	0.2

$^a\Delta g_i = (g_i - g_e) \times 10^3$.